Thermal Modeling and Simulation of Metals Additive Manufacturing

by

Basil Judge Paudel

A thesis submitted to the Graduate Faculty of
Auburn University
in partial fulfillment of the
requirements for the Degree of
Master of Science

Auburn, Alabama
December 14, 2019

Keywords: Additive manufacturing, thermal effects, low fidelity approach, heat transfer
application

Approved by

Dr. Scott M. Thompson, Chair, Associate Professor, Mechanical Engineering
Dr. Sushil Bhavnani, Professor, Mechanical Engineering
Dr. Roy W. Knight, Associate Professor, Mechanical Engineering

Abstract

Additive manufacturing (AM) enables a layer-wise approach to near-net shape fabrication of three-dimensional computer aided designs. In powder-metal-based AM processes, such as directed energy deposition (DED) and laser-powder bed fusion (L-PBF), a laser is used as the heat source to partially/completely melt the powder material. In the current work, both manufacturing processes are numerically modeled to understand the thermal behavior during powder/laser-based AM processes, and the effects of process/build parameters are studied. Common AM materials such as Ti-6Al-4V, stainless steel 316L and Inconel 625 are examined in the current work due to their industrial use. Scan-wise and layer-wise manufacturing effects on heat transfer are quantified via peak melt pool temperature and resulting melt pool morphology. Both powder effects and phase change within the melt pool are considered using approximate, reduced-complexity techniques. The employed numerical model has been validated using data available in the literature. Results demonstrate that the melt pool morphology and temperature distribution along build geometries with negative draft angles are significantly different than those with positive draft angles during L-PBF. Additionally, the proposed analytical model has been successfully validated to predict thermal distribution within the bulk-region of thin walls manufactured via powder/laser DED.

Acknowledgments

I would like to thank my advisor, Dr. Scott M. Thompson, for providing me with this wonderful opportunity to work in this research. His guidance is very much appreciated in the past two years. I would also like to show my gratitude towards my committee members, Dr. Sushil Bhavnani and Dr. Roy Knight, for their support. I am very thankful to Garrett Marshall for his help with some of the prior experimental work. I am very much thankful to my wife, Nisha Bhattarai, and my brother, Yub Raj Paudel, for their encouragement and support along this journey. I would also like to thank Dr. Nima Shamsaei, as well as my current and past lab mates at National Center for Additive Manufacturing Excellence (NCAME) laboratory. Finally, I would like to thank all my friends and family who has directly or indirectly helped me through graduate school.

Table of Contents

List of Tables

List of Figures

Nomenclature

Acronyms

AM   Additive Manufacturing

L-PBF Laser- Powder Bed Fusion

DED   Directed Energy Deposition

DLD   Direct Laser Deposition

HAZ   Heat Affected Zone

SAZ   Substrate Affected Zone

VED   Volumetric Energy Density

LENS Laser Engineered Net Shaping

IR   Infrared

CNC   Computerized Numerical Control

FEA   Finite Element Analysis

PREP Plasma Rotating Electrode Process

Symbols

a   Thin wall length, m

A   Absorptivity coefficient

A_c Cross-sectional area, m²

c_p Specific heat capacity, J/kg-K

d   Melt pool depth, m

Fo   Fourier number

h	Heat transfer coefficient, W/m²K
k	Thermal conductivity, W/m-K
l_{subs}	Substrate thickness, m
l_t	Layer thickness, m
L	Length, m
L{n}	nth Layer, e.g. L1, L2, L3
L_c	Characteristic length, SAZ onset height, m
m	Fin parameter, m^{-1}
n	Number of deposited layers
P	Power, W
Pe	Peclet number
PM	Pyrometer value, °C
Q	Absorbed laser energy, W
R	Laser beam radius, m
R_{th}	Thermal resistance, K/W
R_{sp}	Spreading resistance, K/W
t	Time, s
T	Temperature, °C
V	Laser scan velocity, m/s
x	x-coordinate, m
x_0	Laser Position in x-axis, m
y	y-coordinate, m
y_0	Laser Position in y-axis, m

z z-coordinate, m

Greek Symbols

α Thermal diffusivity

β Overhang angle

Δ Difference

ε Surface to ambient emissivity

ρ Density

θ Phase fraction

Θ Temperature difference

Subscripts

∞ Ambient

active   Active laser status

b   Base of fin

cond   Conduction

dwell   Laser dwell status

fin   Fin

max   Maximum

mp   Melt pool

repos   Laser reposition status

subs   Substrate

tip   Fin tip

Chapter 1: Background

Additive manufacturing (AM) is a layer-wise manufacturing process. Contrary to the conventional subtractive process, where a raw stock is chipped and machined to a pre-designed shape and form, AM relies upon layer-by-layer deposition of material that conforms to the designed part. The track-wise deposition within the layer is guided by a computerized numerical control. While the underlining concept of AM of metals is very much the same, it comes in various forms that can be grouped broadly based on the feed process. The two major types of AM are (i) Laser-based Powder Bed Fusion (L-PBF), and (ii) Direct Energy/Laser Deposition (DED/DLD). Both types of metal processing are based on raw material in the powder form. The L-PBF requires a pre-deposited powder bed prior to selective metal fusion before each layer scan, whereas the DED process blows metal powder using one/multiple co-axial nozzles, e.g. Laser Engineered Net Shaping (LENS®), concurrently melting the powder and depositing the liquid. The primary difference between the two AM processes is the absence of powder-bed in the DLD process. Consequently, the DLD brings added benefits to the repair industry. The DLD process also provides benefits in that the thermal monitoring tools such as infrared (IR) can be used to capture the thermal history of the deposited clad throughout the duration of the build. In the current work, an IR camera along with a dual-wavelength pyrometer is used to validate the analytical model for a thin-wall fabrication using the DLD process. This research uses COMSOL Multiphysics as a numerical tool to model both AM processes and deliberate the findings from the case studies.

1.1. Motivation

In any manufacturing process, it is very important to understand how the process parameters affect the material properties of the end-product. Many conventional processes through decades of research work have identified such relationships which can be used as a go-to resource on demand. Additive manufacturing processes, such as L-PBF and DLD, however, have been only gaining momentum in the last few decades, and severely lack enough understanding of these process maps that tie the process-property-performance relationship. One way of doing so is through numerical simulation of the cladding process. In a typical laser-based AM of metals, several physical phenomena, for e.g. conduction, convection, radiation, melt pool dynamics, spatter, phase-change, and powder dynamics among others, exist as shown in Figure 1. With the knowledge of these phenomena, implications can then be made on the solidification direction, grain size/growth, melt pool stability, residual stress, pore formation, etc. However, a multitude of these physical phenomena makes an accurate, high-fidelity simulation process quite demanding computationally, which even with the current development of computational power is not adequate to model an entire fabrication process. A realistic approach to avoiding such time-delays has been to use effective/lumped continuum-based models. For example, instead of modeling discrete powder dynamics, a continuum modeling approach is considered where the powder bed is assumed as a continuum and is assigned an effective material property (conductivity, heat capacity, density). Similarly, phase changes are accounted for using latent heat values. Even so, due to differences in size/time scales, high-fidelity numerical simulation has been limited to few tracks instead of an entire part. The current work aims to propose a new approach in the thermal prediction of the bulk part in the thin-wall cladding process.
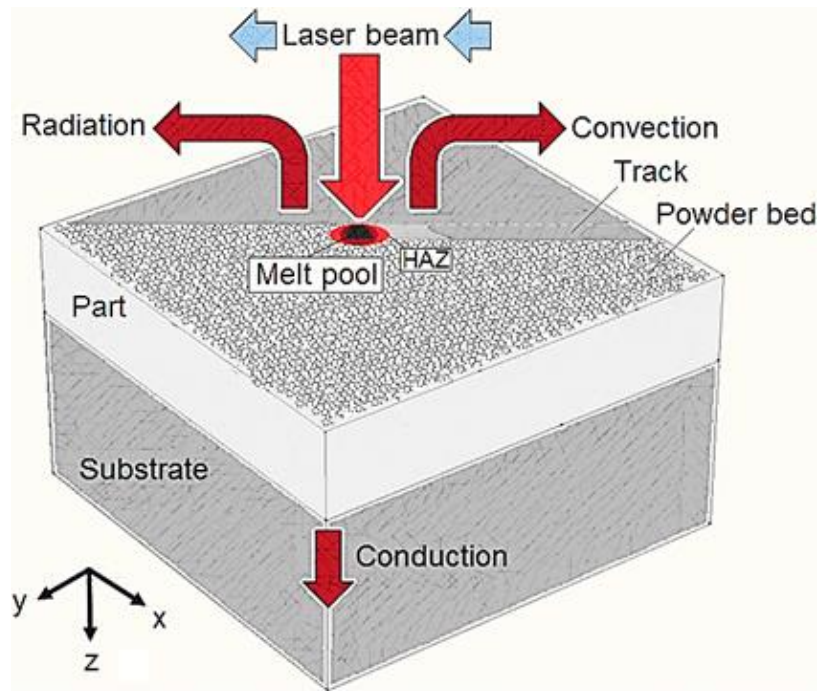
Figure 1: Schematic of thermal phenomena in an L-PBF AM process [1]

1.2.   Objectives

The objective of this work is to study the effects of various AM process/design parameters on the deposited clad. In both AM processes, the effects of a single track, multi-layer scanning are discussed. Results are obtained through numerical and/or experimental studies. These studies provide key information on the melt pool morphology, which along with the thermal history can be used to predict the microstructure, residual stresses in the part. More specifically, the objectives can be summarized by:

1. Study the effects of overhangs (local geometry changes) in the L-PBF process

2. Study the effects of part size during the powder/laser DED process

3. Develop a low-fidelity approach to predict the bulk thermal history in the AM process

3

1.3. Thesis outline

This thesis is presented as a compilation of papers format. The thesis work will demonstrate, through multiple case studies, presented chapter-wise, the effective use of numerical and analytical modeling of the two most common metal-based AM processes: L-PBF and DLD. Chapter 2 presents findings related to the overhang effects on the melt pool morphology and thermal characterization in the L-PBF AM process. In Chapter 3, using thermal monitoring tools, the effects of part size on the thermal history is studied. Additionally, a fast low-fidelity bulk thermal model is proposed for thin-walls in the DLD process, based on the fin-model approach. Chapter 4 summarizes the findings from the case studies and the necessary future work.

Chapter 2:   Overhang Effects in Additive Manufacturing

2.1.   Abstract

The effect of local part topology on the heat transfer during the laser-powder bed fusion (L-PBF) additive manufacturing (AM) process is investigated. The high heat flux diffusion (i.e. thermal spreading) is numerically modeled and investigated for the L-PBF of a thin-walled part with various negative draft angles (overhangs) and a thin wall of variable cross-sectional area. Scan-wise and layer-wise manufacturing effects on heat transfer are quantified via peak melt pool temperature and resulting melt pool morphology. These thermal metrics are used to understand the effect of overhang angles on the melt pool mand the surface roughness traits of stainless steel 316L, Inconel 625 and Ti-6Al-4V parts. Both powder effects and phase change within the melt pool are considered using approximate, reduced-complexity techniques. The employed numerical model has been validated using data available in the literature. Results demonstrate that the melt pool morphology and temperature distribution along build geometries with negative draft angles are significantly different than those with positive draft angles.

2.2.   Introduction

Laser-based powder bed fusion (L-PBF) utilizes a powder bed platform that can change height in increments of micrometers to accomplish layer-by-layer additive manufacturing (AM). A typical schematic of the system [2] is shown in Figure 2. Initially, a coater distributes the metal powder across the build platform. Intense laser irradiation is concentrated at a micron-sized spot in order to provide sufficient energy to melt the powder. As the laser moves with a speed on-the-order of ~1 m/s per instructions from computerized numerical control, the melt

pool quickly solidifies and creates a track of solid metal which is repeated over numerous patterned tracks to form a complete layer. To form a complete 3-dimensional part, the build platform then lowers by the specified layer thickness. This process is re-iterated for several slices of the input design resulting in a part with near net shape and relatively fine quality. More recently, AM technologies such as L-PBF have gained traction in industry for engineering material with unique specifications while minimizing supply chain costs. Employing AM technology provides benefits from the consolidation of multiple phases in material production into a simple process. Another advantage of L-PBF comes from the re-usability of the un-used powder resulting from the un-sintered powder bed. Despite these clear benefits, this relatively new technology still has complications that arise, mainly due to the fast-moving, small-sized laser heat source.
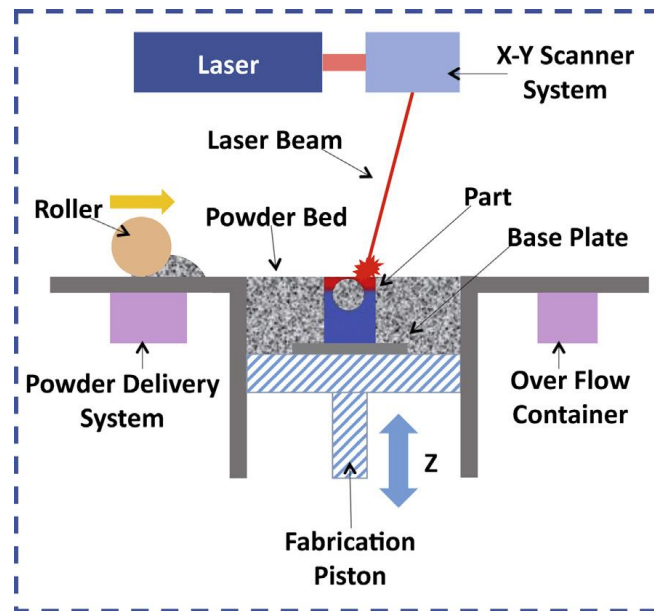
Figure 2: Schematic of an L-PBF process system [2]

Engineering a customized part requires knowledge of a material's thermal history from the melting to solidification phases. With the proper physical modeling, one can determine the

temperature distribution and gradients within the part for estimating the evolution of the material structure during AM. While this is easier said than done, challenges await in the ability to predict the thermal history and cooling rates due to opposing scales associated with the heat source size and velocity, respectively. Analytical solutions for the melt pool and heat affected zone (HAZ) temperature distributions have been developed, or in some cases modified, from the solutions pertaining to welding applications. The earliest solution dates to Rosenthal [3] for the moving point heat source on a semi-infinite solid. However, Rosenthal's model and its predecessors are generally limited to standard geometries with very simple shapes. To ease computations for various practicing engineers, researchers have developed 'process maps' [4–6]. These maps provide a 2D/3D visualization of analytical models – providing relationships between temperature, mechanical properties and process parameters for assisting the AM process design. More recently, there has been an overwhelming amount of numerical studies performed to better understand the multi-physical processes involved during L-PBF [7–12].

In general, the quality of any fabricated, metallic part depends on the process parameters used in the manufacturing process. For L-PBF, the major process parameters that affect part quality are laser power, scan speed, hatch spacing (distance between two laser tracks), layer thickness, build orientation, and part position within the platform [2]. Dimensional or non-dimensional groupings of parameters such as the volumetric energy density (VED), *Peclet*, *Marangoni*, *Biot*, and *Fourier* numbers can be used for process mapping for predicting process-property relationships more agnostically. For example, a low energy density may result in low-quality parts due to the presence of lack of fusion (a consequence of insufficient energy to melt powder) and/or voids, while high energy density increases warping and spatter generation [13].

Many research studies have concentrated on predicting the melt pool shape and size during a single-layer L-PBF process simulation. Multi-pass laser simulation studies have found very little traction in research due to computational time required to perform such multi-physical approaches. In general, multiphysics approaches involving powder, liquid melt pool or laser-powder-melt pool interactions have been limited to single track simulations [11,14–17].

One of the most overlooked process parameters in L-PBF is the build orientation. Multiple studies [18–20] reported the inability of L-PBF, also AM in general, to produce consistent microstructure in the part. Yadollahi et al. [20] studied the fatigue performance of additively manufactured stainless steel 17-4 PH in different build orientations and attributed the drop in the performance to the direction of the un-melted plane between layers with respect to the loading direction. While those results show some evidence to the difference in performance, Hartunian and Eshraghi showed inherent differences in the microstructure resulting due to the orientation of heat-dissipating direction. Their study also pointed out that the horizontally built samples close to the substrate presented brittle fracture features while the ones away showed ductile fracture features. Simonelli et al. [21] studied the microstructure and fatigue performance of L-PBF Ti-6Al-4V, however, they reported that for the specimens tested, no difference exists between specimens at varying distances from the substrate. They also observed predominant columnar grains in the fabricated part and attributed it to the track-wise and layer-wise nature of the AM process.

Fox et al. [22] studied the effects of surface angle (with respect to the horizontal build plane) on the surface roughness of L-PBF parts. The study showed that surface roughness (R_a) increases with increasing overhang angles. While these results are consistent with what has

generally been reported in the literature, these authors concluded that a definite correlation between the surface angle and the R_a does not exist.

Build orientation is a design parameter for AM and is known to affect the final material properties as well as part performance. For example, specimens built at 45º to the horizontal plane (i.e. substrate) were found to have greater surface roughness; resulting in earlier fatigue failure [20]. However, in a microscale, any layer fabricated on top of powder particles instead of solid clad can be treated as an overhang. A schematic of a localized overhang region anticipated in the layer-wise manufacturing process due to varying cross-section area is shown in Figure 3. While numerous studies have shown performance differences due to build orientation, the thermal phenomena/characteristics within impactful regions have rarely been characterized. This current study focuses on the effects of negative draft angles and part overhangs, characterized by an overhang angle, on the peak temperature, bulk/sensible heating and t melt pool shape along a part. The study focuses on the L-PBF of Ti-6Al-4V, stainless steel 316L, and Inconel 625 (IN625) - which are all typical materials used for metals AM.
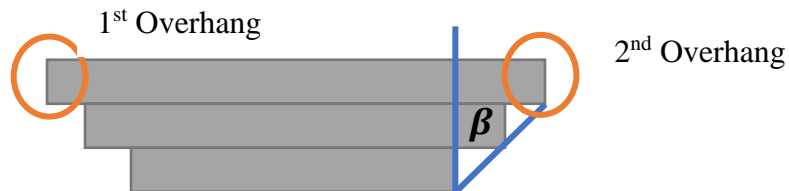
Figure 3: Schematic showing 1st and 2nd overhangs in subsequent layer scans during fabrication of a single-track, thin wall with a negative draft angle
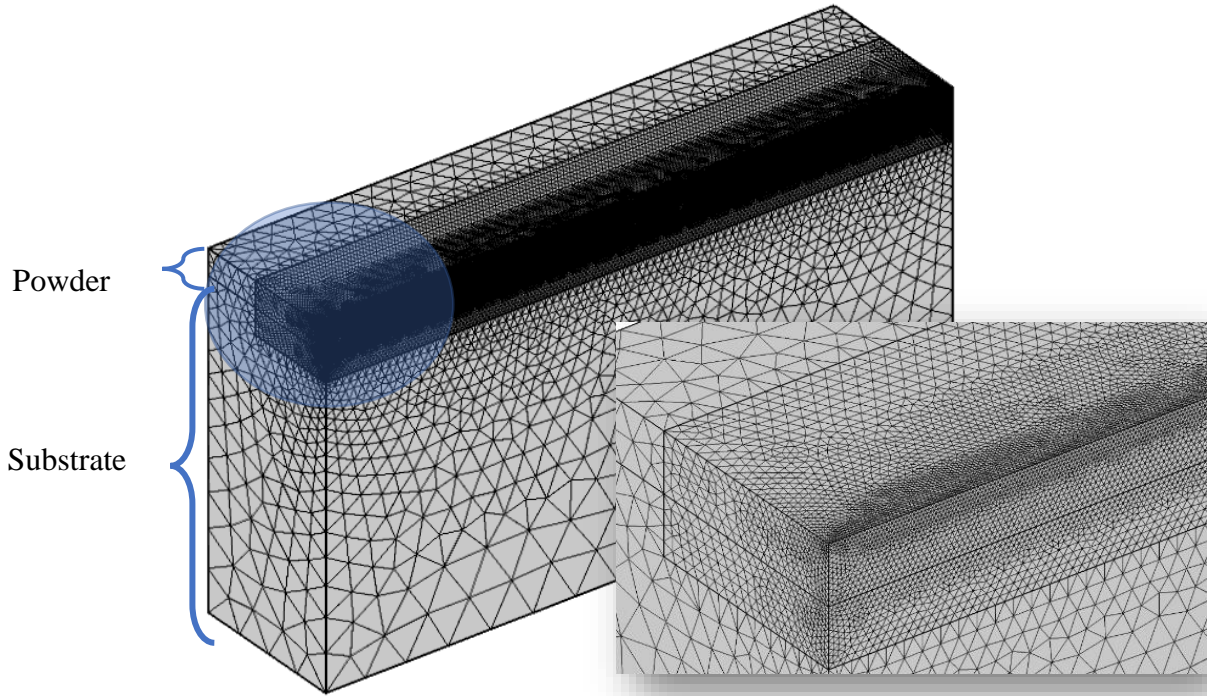
Figure 4: Mesh used for multi-pass study at an overhang region

2.3. Problem setup

Numerical studies were conducted for three materials commonly used in the AM industry: Ti-6Al-4V, IN625, and stainless steel 316L. All numerical simulations were performed using the commercial software package, COMSOL Multiphysics 5.4, on the Hopper supercomputing cluster at Auburn University. The thermophysical properties for each material were taken from the open literature [23–25]. Initially, single-pass simulations ware tested for IN625, and results validated against the experimental data from Ref. [26]. Numerically predicted and experimentally measured melt pool dimensions are tabulated in Table 1 for two different laser scan speeds. For both validation studies, a nominal laser power of 195 W was used. The scan speed was set at 800 mm/s for Case A, and 500 mm/s for Case B. The laser was modeled using a Gaussian beam intensity that decays exponentially with distance from the center. The

numerically-predicted melt pool dimensions were found to agree within 10% of the experimental

values for both cases as shown in Table 1. As expected, the melt pool dimensions decreased with

increasing scan speed. Discrepancies between numerical and experimental values are partially

attributed to the uncertainty in absorptivity (0.35 is currently used for absorptivity by the

substrate surface) and material properties for the liquid state. The numerical study consistently

overpredicted the melt pool dimensions for both cases. However, since the current study only

concentrates on the qualitative trends results from relatively slight process parameter variation,

no further adjustment was deemed necessary. Mesh independence studies were performed and no

significant changes in melt pool dimensions were found. The mesh used for multi-pass

simulations is shown in Figure 4. A similar meshing scheme is used for remaining studies within

this chapter. Due to the adaptive time stepping feature, time steps were dynamically adjusted to

finer step sizes, as small as 10^{-8} s, during abrupt load changes, such as during the start and end of

the scan within a track. This feature allowed for the rapid computation of the solution during the

cooling phase (dwell time).

Table 1: Comparison of melt pool dimensions between simulation and experimental data [26] for single-pass study

		Experimental (µm)	Numerical (µm)	% Error
Case A 800 mm/s	Melt pool width	133.0	134.3	1.0 %
	Melt pool depth	38.0	40.8	7.4 %
	Width/depth ratio	3.5	3.3	6.0 %
Case B 500 mm/s	Melt pool width	162.0	154.8	4.4 %
	Melt pool depth	49.0	50.0	2.0 %
	Width/depth ratio	3.3	3.1	6.1 %

The current study accounts for powder presence at a continuum scale using a modified thermal conductivity value. The powder bed thermal conductivity was taken as ~1-2% of the solid value based on relations proposed in the literature [27–29]. Through the usage of the 'Irreversible Transformation' feature provided by the software module, which keeps track of the material form, the current study accounts for the powder to melt pool transformation (irreversible) and liquid to solid form through phase change phenomenon. This combination allows for a more convenient phase tracking in the module. The powder to melt pool (irreversible) transformation was designed to occur when the local powder temperature exceeded the liquidus temperature for at least a tenth of a millisecond ($100 \, \mu s$). The time step was determined based on the characteristic melting time for a mean powder size of $20 \, \mu m$ via the relation $t = L^2/\alpha$ as a first approximation. Both radiation and convection heat transfer losses along the top surface of the powder bed, as well as the exposed solid surfaces, were accounted for. A convection coefficient of 15 W/m^{2}K was used to model forced convection within the build chamber and is within the range of values reported in the literature [17,30]. The symmetry boundary condition is applied whenever possible to reduce computational time. For all cases, the substrate temperature was set to 20 °C except for the initial validation study where the model followed similar boundary conditions as the reported experiment. Powder absorptivity values were taken from Ref. [31] for IN625 (0.65), SS 316L (0.65) and Ti-6Al-4V (0.71), and are usually reported to be ~2-7 times higher than the flat surface absorptivity due to powder shape, surface roughness, and oxidation.

The peak melt pool temperature was found to become steady within a fraction of a millisecond. As such, the transient study was conducted for an L-PBF track length 10 times the beam radius to save computational time. The clad was then allowed to cool off for a duration

equal to 25 times the track duration during which the average clad temperature cools down to a tenth of melting point temperature. Other simulation parameters are listed in Table 2. For the subsequent layer, the laser scans from the first overhang along the clad beneath and ending at the second overhang. The simulation of three single-track layers during the overhang study of each material took around 168 hours using 20 processors.

Table 2: Simulation Parameters for L-PBF process

Materials	Ti-6Al-4V	IN625	316L
Substrate temperature	20 °C		
Laser power	100 W		
Scan speed	500 mm/s		
Beam diameter	140 µm		
Layer thickness	40 µm		
Hatch spacing (for multi-pass)	0.1 mm		
Track length	0.7 mm		
Time between successive passes	25× track time		

The employed numerical model utilizes material properties definition from the literature data referenced earlier. Due to experimentation error at high temperatures, approximately 15% of uncertainty was reported. Consequently, this along with other assumptions in the modeling process, such as a uniform convection coefficient, neglecting of melt pool dynamics, truncation error from CAD/meshing, uniform emissivity assumption, may add to the error in the calculations as such properties were measured during less-drastic conditions. However, for a

qualitative analysis under similar material and environment conditions, the observed trends can be considered representative of the physics.

2.4. Results and discussion

2.4.1 Multi-pass effects

This current multi-pass L-PBF study shows that the melt pool dimensions increase significantly between the first pass and the subsequent passes within the same layer, and has the potential to stabilize over time. The stabilization in melt pool size tends to be associated with longer tracks. Shorter tracks, for example, when checkerboard scan patterns are being used or when the track length available is small due to part thickness in the direction of laser scan, may not allow for such stabilization, and this can leave the entire layer with non-uniform melt pool dimensions, as has been observed in the published studies.

The ability to predict the melt pool shape along with the cooling rate and thermal gradient is particularly important in understanding grain evolution within a part. Most studies that rely on single-track L-PBF simulations show symmetric melt pool shapes. However, in practice, this may only exist for the first few tracks of a layer partition/island. With multiple passes, the already solidified clad on one side and the powder on the other side of the track, conduction heat transfer occurs unevenly, mostly on the side of the already solidified track. As a result, the instantaneous melt pool shape is highly asymmetrical, as shown in Figure 5. Additionally, in the depth-wise direction, the melt pool shape becomes flatter due to the presence of a powder bed on the side.
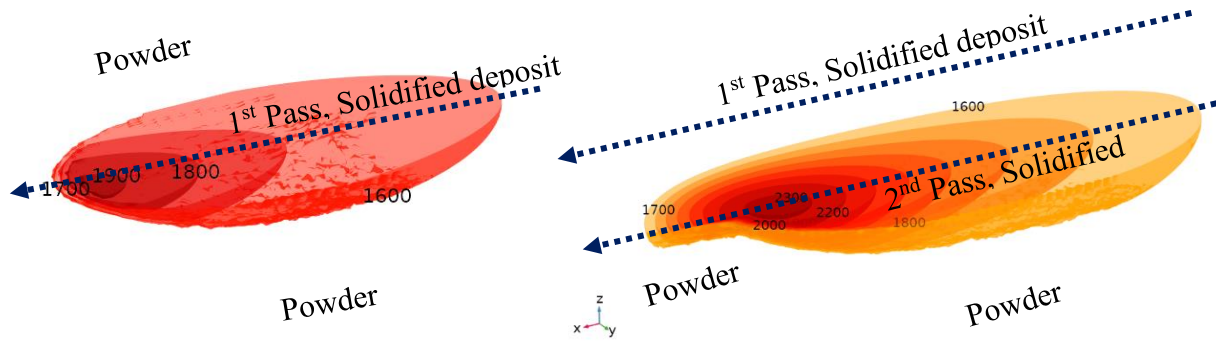
Figure 5: Simulated melt pool shape isothermal contours (in ℃) resulting from single track vs. multi-track laser scan in IN625 (arrows show the path of the laser beam center and scan direction)

2.4.2 Multi-layer scanning and overhang effects

The melt pool when the powder material sits beneath the layer under processing has also been investigated herein. This scenario occurs during the L-PBF of a part with overhangs; with overhang orientation quantifiable via an overhang (or draft) angle. The thermal phenomenon during L-PBF of the overhang is quite unique in the sense that energy dissipation occurs through a limited interfacial surface area. This results in more constrictive heat flow through the melt pool which contrasts with the thermal spreading that occurs on builds with positive draft angles. There is a high thermal resistance associated with the low thermal conductivity of the powder surrounding the melt pool in the overhang region.

The instantaneous melt pool dimensions for three consecutive laser passes for an overhang angle of 60° are shown in Figure 6. The first laser pass is done on the substrate and consisted of no overhangs. The x-axis represents the time since the start of the track and resets with each new layer. The melt pool dimensions (half-width, and depth) are shown in the primary y-axis, whereas the peak melt pool temperature is shown in the secondary y-axis. The results

from the single track, multi-layer study, with a scan speed of 500 mm/s and an absorbed power

of 60 W, show that the melt pool width does not change significantly between subsequent laser

passes. However, melt pool depth increases considerably at the overhang region between the first

pass and the second pass. A second case study on IN625 was performed with increased scan

speed of 800 mm/s and higher absorbed power of 120 W. Results for this scenario (not shown)

show that both the melt pool width and depth have similar trend – unlike what was observed for

the previous case with 500 mm/s and 60 W, and worthy of further investigation but not included

in this study.

The melt pool depth was found to not increase as much after the third pass during L-PBF.

It was found that there is a slight pull down on the melt pool depth dimension around 40 µm

which corresponds to the powder layer thickness. The slight resistance towards deepening the

melt pool is due to the powder-transformed-melt-pool meeting the cooler solid substrate/deposit

which is capable of higher heat transfer rates. Likewise, the overshooting of the melt pool depth

can be explained by the fact that at the overhang region, the laser thermal energy only penetrates

72 µm through the powder due to its substantially low thermal conductivity. As soon as the laser

beam scans the region with solid mass beneath the powder layer (non-overhang region), the melt

pool depth sinks suddenly due to the higher heat transfer rate provided by the solid clad. This

sudden quenching of this melt pool in the overhang region may consequently affect the material

properties resulting in a more brittle partial region/surface within the fabricated part. These

changes in the melt pool geometry can be considered solely due to the overhang effects. This

shows that the L-PBF of overhang structures is a highly localized process isolated from the

effects of substrate temperature or bulk heat accumulation in the cladded region. In the non-

overhang region, the melt pool dimension (width and depth) increases slightly with subsequent layers due to bulk heat accumulation.
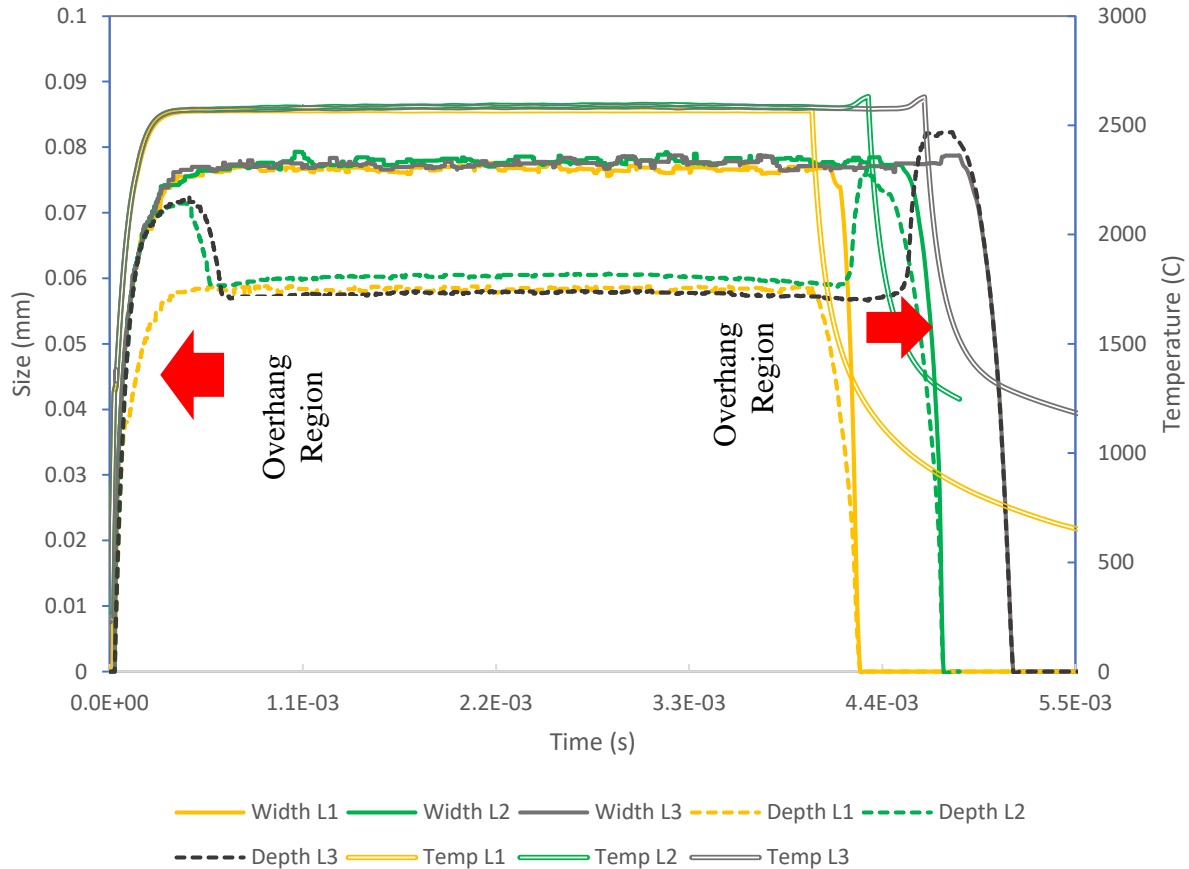
Figure 6: Melt pool dimensions and maximum temperature for the first (L1), second (L2) and third (L3) laser pass for IN625 at 500 mm/s scan velocity and 60° negative draft angle

It was found that the melt pool morphology at an overhang at the end of the track differs from the first overhang leading to different temperature distributions within the melt pool and HAZ. Melt pool formation at the beginning of the track consists of first superheating newly deposited powder initially at room temperature to melting temperature in order to fuse with the previous layer. In contrast, during the formation of the clad at the end-of-track overhang (2nd)

region, a fused melt pool already exists on the tail region of the newly formed overhang. Since the tail is already above the melting temperature of the powder, absorbed laser energy enables more powder to melt in the overhang region. This allows for the end-of-track melt pool to grow even larger than the one at the beginning of the track (1ST overhang).
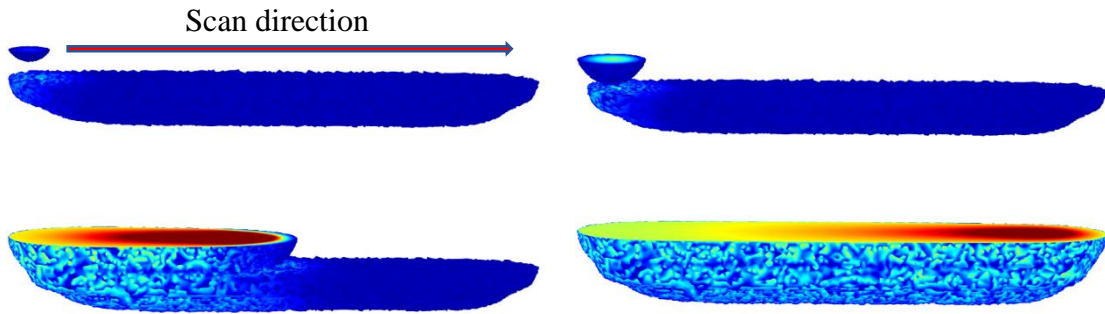
Figure 7: L-PBF of a clad along the second layer for overhang of 30° in IN625 at different time steps of melt pool formation; top-left shows melt pool nucleation on top of powder, top-right shows melt pool fusion with previous layer, bottom-left shows progressive melt pool, bottom-right shows final melt pool
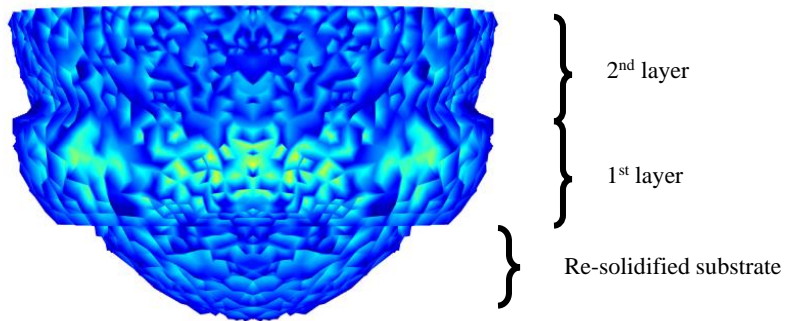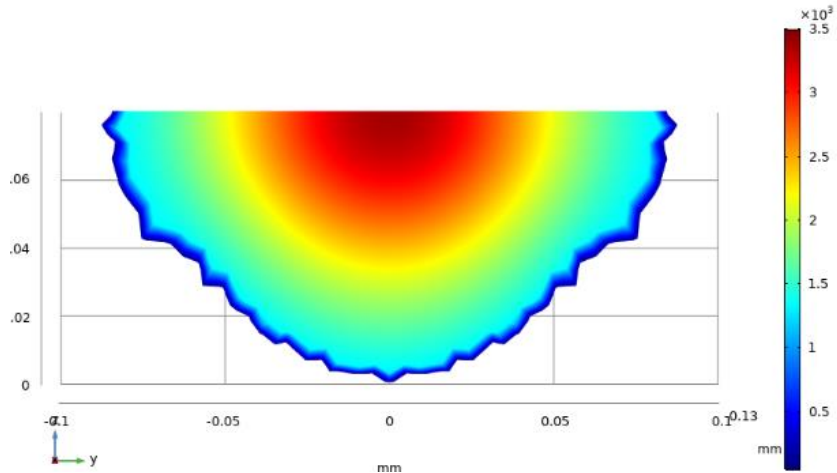
Figure 8: Multi-layer single track bead view (top) of melt pool showing re-solidified substrate, first layer and second layer of deposit (unmelted powder and substrate not shown); and melt pool temperature profile (bottom) halfway during second layer scan

Figure 7 shows the melt pool during the L-PBF of a new IN625 layer on top of an existing solidified layer with a 30° overhang angle for a track length of 0.7 mm. The color map represents melt pool temperature, except when blue which represents the solidification boundary. It may be seen that, during the first few microseconds, a disconnected melt pool is formed which grows and ultimately fuses with the previously formed clad. The maximum melt pool temperature during the laser scan along the part/powder does not change considerably in subsequent passes. This is because of inter-layer dwell time after each layer scan and the addition of fresh powder at room temperature. Similarly, due to low powder conductivity and the time scale associated with the process, the top surface of the powder bed can be considered thermally isolated from the deposited clad. Consequently, maximum thermal energy is stored at the top layer of the powder bed. Similarly, Figure 8 shows the width-wise morphology (top) of the solidified clad after deposition of two single-track, multiple layers on top of the substrate, and melt pool temperatures (bottom) during the middle of 2nd layer.

19
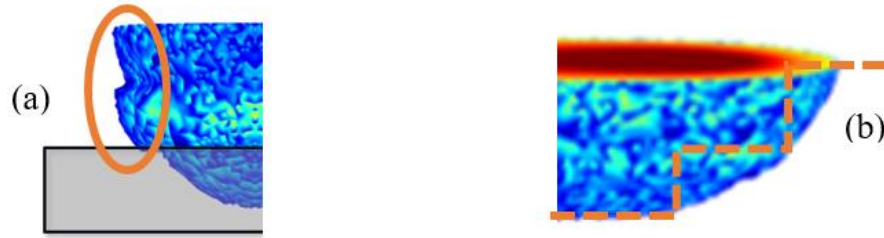
Figure 9: Illustrations showing (a) surface irregularities, and (b) staircase effects in multi-layer L-PBF process

The width-wise direction of the melt pool, as shown in Figure 9(a), shows more irregularities with respect to each successive layer. Although this does not immediately affect the undersurface of the overhang, this effect is present in most layer-wise additive processes even for parts built vertically-upward with zero draft angle. These irregularities or ledges arising from the layer-wise scan may contribute to the overall surface roughness of the final part. This effect is more pronounced when the layer thickness approaches the maximum melt pool dimensions for the selected powder material and process parameter combination. Conversely, when the power is high enough giving rise to higher melt pool dimensions, this quenching effect may not be as visible due to earlier contact with the solid deposit. The effect of power and velocity will be a task for future studies.

The peak melt pool temperature during the first and second laser scan for stainless steel 316L at various overhang angles is plotted in Figure 10. It may be seen that no significant change in maximum temperature occurs within the overhang region as compared to the non-overhang despite the difference in angles. For an overhang angle of 60º and for stainless steel 316L, the increase in maximum melt pool temperature is 0.6% of the value at the non-overhang region for the first overhang layer, whereas it increased to 1% at the second overhang. For lower

draft angles, the increase in temperature was less than 10 °C (<0.1%), and within the numerical margin of error. Similarly, the melt pool width did not seem to be affected solely by the overhang angle for the parameters tested against. In general, the results demonstrate that for chosen laser scan speed, power, and material, no significant difference in peak melt pool temperature exists at the overhang although a slight increase in temperature occurs in successive layers due to bulk heat accumulation as shown in Figure 10.
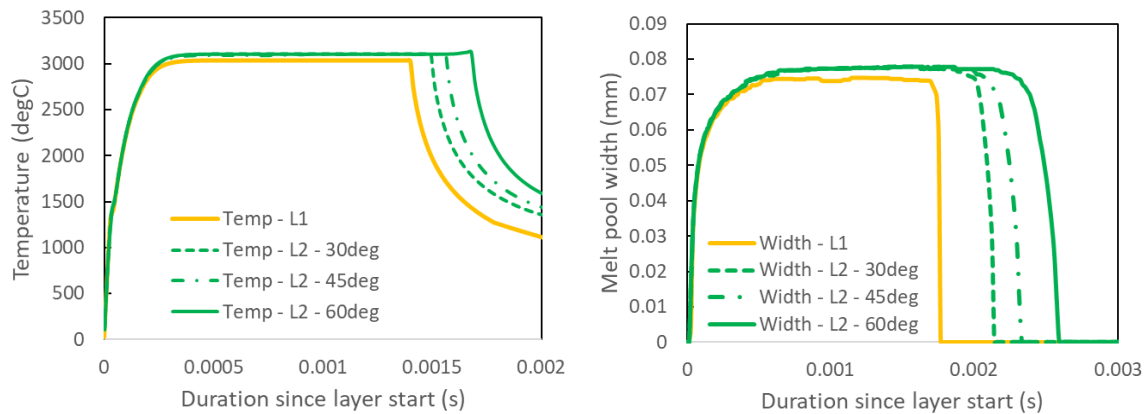
Figure 10: Comparison of peak melt pool temperature (left) and width (right) between the first layer (L1) and second layer (L2) for different overhang angles on stainless steel 316L; L1, L2 in the legend refers to data from layer 1 and layer 2 respectively.

For a given material the melt pool depth was found to be affected by the degree of overhang (overhang angle). The evolution of melt pool depth at different layers, overhang angles, and powder material are tabulated in Table 3. Results indicate that no significant variations were realized at 30° overhang angles, although the melt pool temperature distribution at the end-of-track overhang has a slight spike in the value. By a 45° overhang angle, both start-of-track and end-of-track overhangs showed an increase in melt pool depth. The melt pool at the start-of-track overhang was found to be smaller than the one formed at the end of the track. This

can be attributed to the initial thermal transiency within the melt pool and direction of the laser scan. A deeper melt pool seems to be formed for a longer amount of time at the end-of-track overhang region. With increases in the overhang angle, the difference in the melt pool depth appears to narrow between the two overhangs each lasting for a comparable amount of time.

Table 3: Comparison of melt pool depth at different layers and overhang angles (β) on various powder bed materials

30 °	45 °	60 °
SS316L		

| IN625 | | |
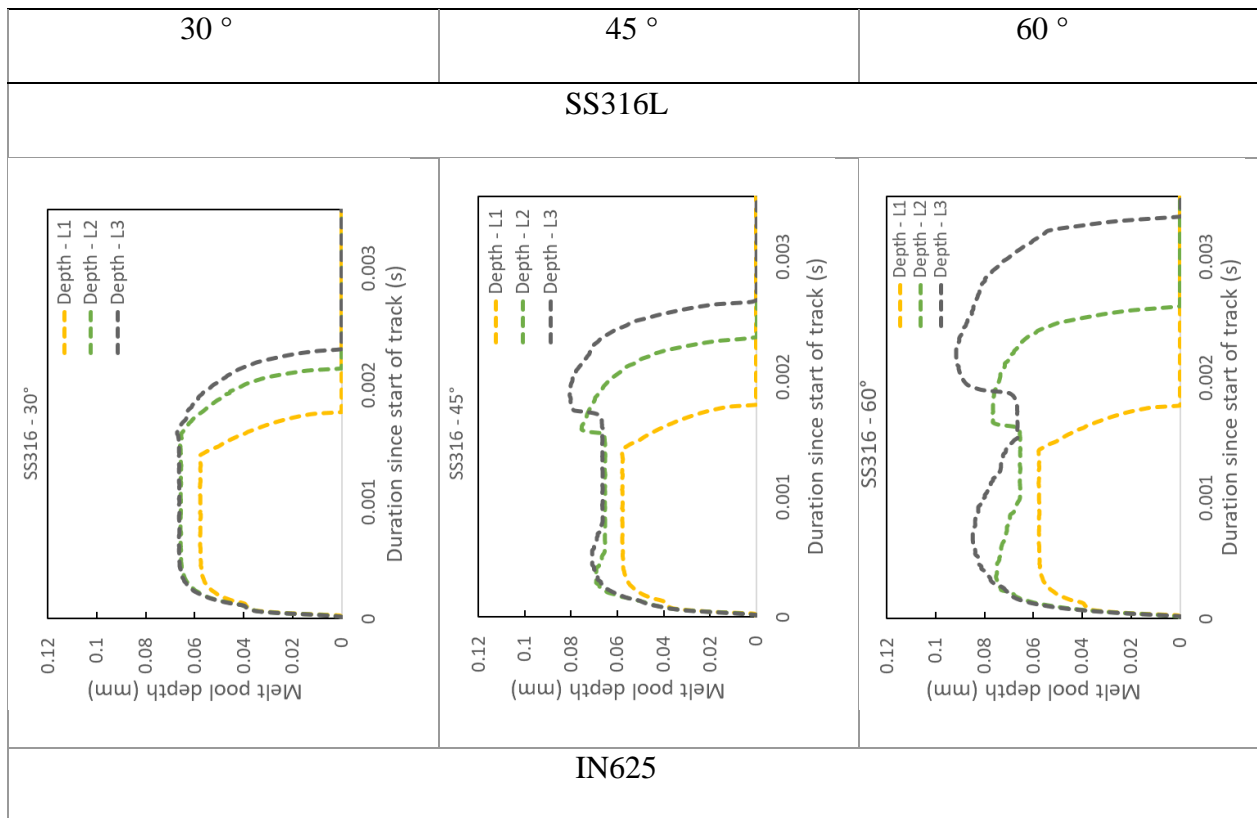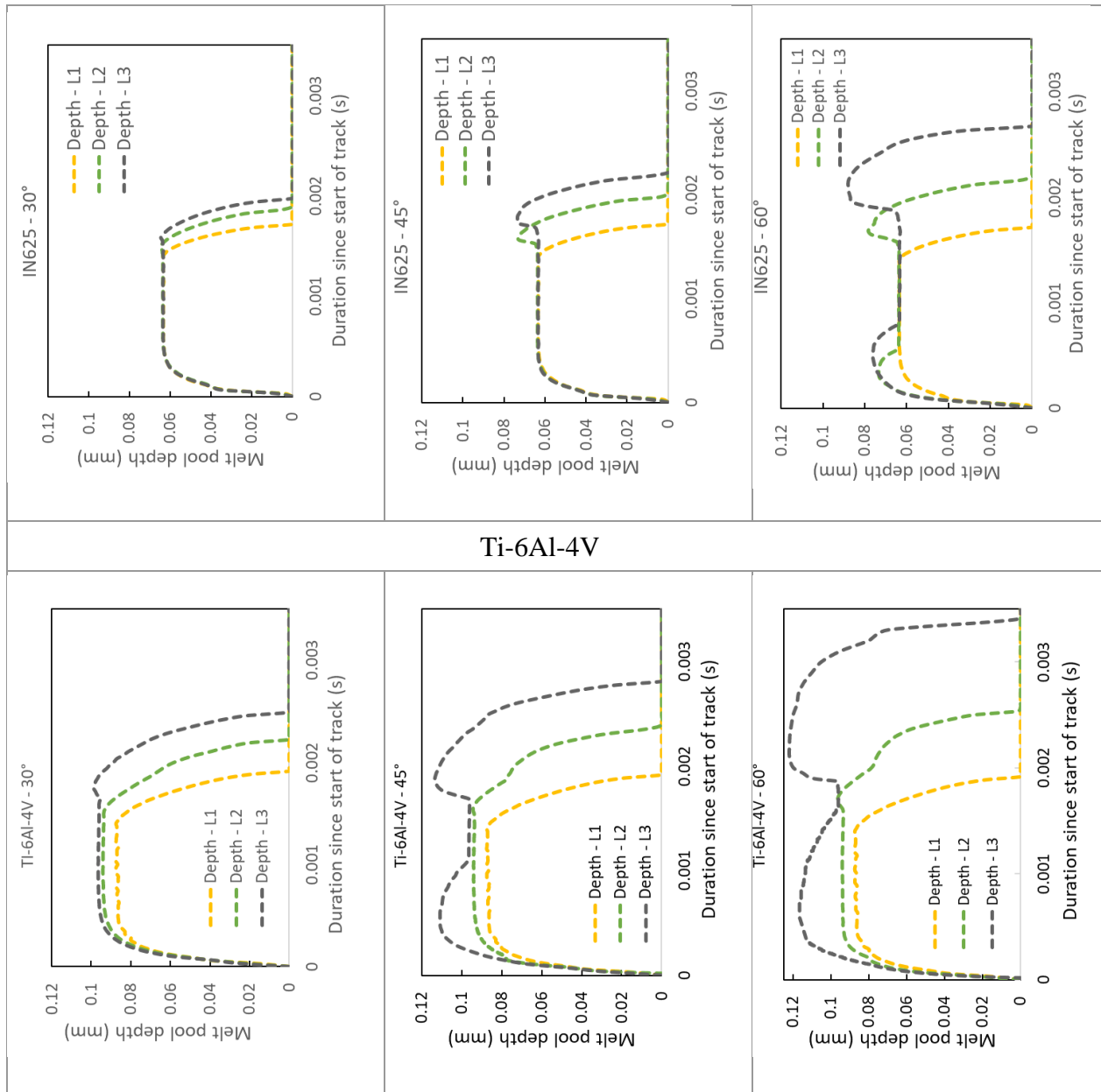
For a relatively low overhang angle of 30°, low surface roughness is predicted by the model in the overhang surface. To some extent, any staircase effects may be somewhat 'minimized' by the melt pool when fabricating overhang structures as shown in Figure 9(b). Deeper melt pools in the overhang region affect the expected dimensional accuracy of the fabricated part. Regions with overhang structures may fall out of tolerance due to increased melt

pool depth. While it is commonly understood that dimensional inaccuracy of L-PBF parts with overhangs has been due to the lack of support underneath, the results herein provide additional reasoning based on the local heat transfer within the overhang region.

Table 4: Percentage increase in melt pool depth at the overhang region at 2nd and 3rd layers

Angle (β)	SS 316L		IN625		Ti-6Al-4V	
	2nd Layer	3rd Layer	2nd Layer	3rd Layer	2nd Layer	3rd Layer
30°	0.9%	1.5%	2.1%	2.2%	0.1%	2.5%
45°	15.2%	21.4%	15.1%	16.3%	0.4%	18.0%
60°	18.1%	38.0%	22.9%	39.1%	2.6%	27.1%

Results also indicate that at higher overhang angles, the melt pool depth increases in the vicinity of the overhang. This is due to the high thermal resistance of the surrounding powder bed in the overhang region. Similarly, a comparison of the melt pool depth, as shown in Table 4, between overhang on the 2nd layer and the 3rd layer, shows a significant increase in melt pool depth (in excess of 20%). This is attributed to the fact that during the L-PBF of the second overhang (third layer), the melt pool is formed next to the previous overhang. As a result, the subsequent melt pool (second overhang) heat transfer experiences higher thermal resistance from the solid overhang as compared to the melt pool formed in the earlier layer. Unlike the other two materials, Ti-6Al-4V does not show a significant change in the melt pool dimension in the first overhang. This may be the result of a high melting point temperature and the absorbed power combination. Surprisingly, the absorbed energy overwhelms the material in the subsequent overhang resulting in a similar increase in the melt pool depth.

The simulation results for multiple materials demonstrate that the melt pool shape and geometry does not change much for overhang angles less than 30°. As observed, the melt pool depth increases with higher overhang angles. However, the exact trend in this melt pool dimension may vary with the material. It has been shown that the subsequent overhangs allow reduced thermal dissipation due to low powder conductivity and store more energy thus producing deeper melt pools compared to the one formed in the initial overhang layer. More research is required to be able to predict the relation between material properties and the melt pool dimension.

2.5. Conclusions

The heat transfer as a result of the L-PBF heat source interacting with the powder bed and solidified part consists of phase-change, melt pool dynamics and complex thermo-fluid phenomena – requiring the use of numerical simulation to understand process-property relationships for various metals. The effects of part orientation on this heat transfer can affect part quality – especially when parts have overhangs. The current work highlights the findings on the resulting melt pool that occurs as a result of negative draft angles. The following conclusions have been found for single-pass and multi-pass L-PBF of IN625, SS 316L and Ti-6Al-4V as laser powers 100 W and scan speeds of 500 mm/s:

1) The melt pool width does not depend heavily on the overhang angle.

2) The maximum melt pool temperature slightly increases with a higher overhang angle.

3) Melt pool depth is very sensitive to the overhang angle. However, more work is needed to determine the number of subsequent layers in which the melt pool morphology stabilizes near the overhang region.

4) For overhang angles less than 30°, no variation in pool depth occurs.

5) Surface roughness characteristics and dimensional accuracy in the overhang region can be partially attributed to the unique thermal phenomena at the overhang region.

Chapter 3: Size Effects and Modeling of Bulk Temperature

3.1.   Abstract

Direct laser deposition (DLD), a layer-wise, additive manufacturing process, is a blown-powder directed energy deposition (DED) process. Due to the absence of powder-bed in the chamber, this process heavily benefits the repair industry. Additionally, it allows thermal monitoring tools such as infrared (IR) camera to observe the bulk surface temperature of the cladded body. This chapter presents observations in the effects of part size on thin-wall deposition in the substrate. In this work, Ti-6Al-4V is used as a raw material due to its common industrial use (e.g. biomedical, aerospace sectors). Results indicate that longer walls allow for increased cooling time and a slow thermal "build-up" within the deposited clad. Additionally, the paper presents an analytical approach to predict the temperature distribution within the bulk of the thin wall. The proposed model is validated against the experiments conducted in-house using the IR data, as well as against the literature. The results from the proposed model agree within 15% of the validation experiments.

3.2.   Introduction

Laser Engineered Net Shaping (LENS^{TM}) is a blown-powder, laser-based DED, or Direct Laser Deposition (DLD), additive manufacturing (AM) process for metal part fabrication and/or repair [32,33]. During the LENS process, a laser irradiates and rapidly melts metal powder injected from multiple nozzles attached to a deposition head to a site atop a CNC-guided substrate/platen that moves at a predefined speed and path. The melted metal, or melt pool, continues to be agitated by the injected powder and rapidly solidifies to form a track as the

deposition head moves onward. To form additional layers of the part, the relative distance between the substrate and deposition increases, and the process is repeated. A part is thus fabricated track by track and then layer by layer, in free space. This is in contrast to the laser powder bed fusion (L-PBF) AM process which employs a pre-deposited bed of powder that is then selectively fused. A schematic of the DLD process is shown in Figure 11 [2]. Note that due to the absence of a powder bed, a DLD system allows for the integration of external monitoring tools such as an IR camera to look at the temperature profile of the deposited clad surfaces throughout the build duration. Additionally, an inline melt pool monitoring solution such as a pyrometer can be used to monitor the melt pool.
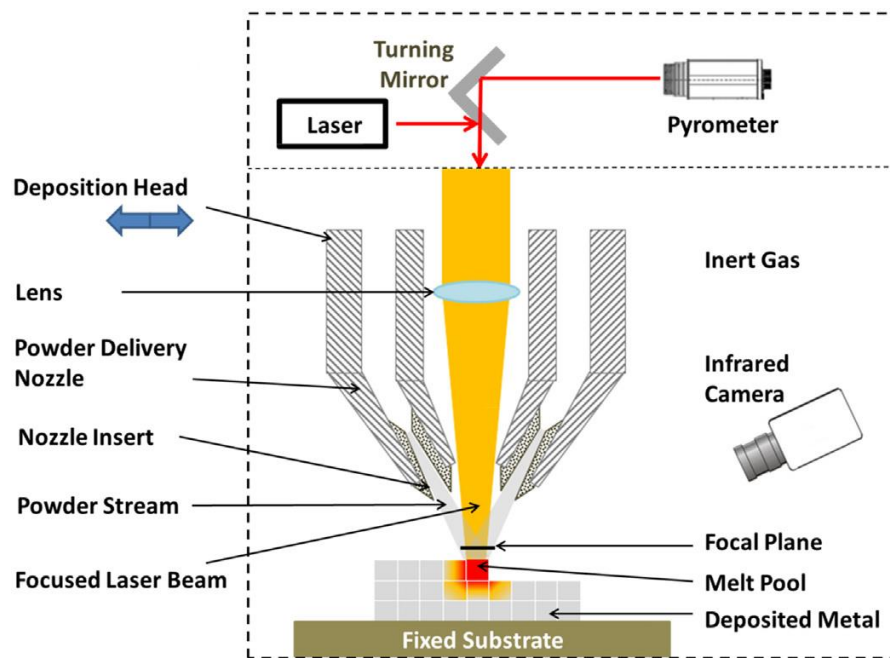
Figure 11: Schematic of a DLD process showing external monitoring tools [2]

Direct Laser Deposition offers the ability to control microstructure [34–36], fabricate parts of higher strength than wrought [37–40], repair/resurface [41,42] and fabricate functionally graded parts [43,44]. A challenge still exists, however, in relating during-the-process heat

28

transfer with a part's size/geometry for various process parameter groupings. Meaning, the same set of process parameters optimal for fabricating a fully dense cylindrical bar may not be ideal in producing a larger, more complex-shaped part of the same material. It is thus vital for one to understand and simulate the DLD process for learning process-structure-property relationships. To obtain these relationships one can directly measure various thermal phenomena during processing, such as a part's thermal response. By understanding a material's thermal response during DLD, one can, for example, predict and better control the final microstructure and residual stress [39,45]. Using the initial cooling rate and temperature gradient, the initial solidification rate can be determined. The local thermal gradient, during the first pass, as well as subsequent laser passes, combined with the cooling rate after the initial solidification, can be used with conventional solidification maps for predicting grain size and type.

Part size and geometry can influence the optimal DLD process parameter selection. The thermal capacitance of the assembly-under-construction, as well as track-to-track time intervals [46,47], will affect heat fluxes and temperature histories, and thus, final material properties. Qiu et al. demonstrated that the successful DLD of larger Ti-6Al-4V requires decreases in the step height increment taken by the deposition head between layers; otherwise, a part falls short of targeted height requirements [48]. The time interval between deposits, which includes any intentional 'dwell' time of the deposition head located away from the part, can be controlled via laser scan strategies and machine programming. Keist et al. [49] experimentally characterized the anisotropic behavior between samples of Ti-6Al-4V deposited as either cruciform or half-cruciform structures. It was found that the tensile properties varied significantly between the thin-walled cruciform and half-cruciform structures, with the variation in dwell time being a contributing factor. Similar results were demonstrated by Yadollahi et al. [46] by varying the

number of fatigue specimens (316L stainless steel) fabricated per substrate. It was shown that increasing the number of specimens lengthens the inter-layer time interval resulting in higher cooling rates. Hence, the parts fabricated as part of an assembly were found to have increased hardness, tensile strength and fatigue life [46].

3.2.1 DLD modeling

To predict the thermal response of LENS materials during manufacture, one may resort to numerical simulation or analytical modeling to solve the heat equation for heat transfer in successive layers. In addition to thermal exchange with surroundings (including laser and chamber gas/walls) via radiation and convection, melt pool formation, fluid mechanics and solidification may also be considered at various scales and fidelity. Analytical solutions are desirable in that they provide insight into thermal phenomena, e.g. bulk cooling rates and temperature gradients, inherent to the process. Perhaps the most well-known of these is Rosenthal's solution to the heat equation for a moving point heat source on a semi-infinite plane [3]. Originally intended for welding, the solution has since been applied to DED due to process similarities and has helped engineers understand how the melt pool geometry and solidified microstructure depends on major process parameters [34,50,51]. Neither latent heat of fusion effects nor temperature-dependent properties are taken into consideration through Rosenthal's approach, and several researchers have noted the need for such information to be integrated for obtaining more accurate solutions [50,52,53].

Applying welding models to the DED process has its challenges and limitations. Most models do not include mass addition to the melt pool or effects of laser attenuation due to powder flow. Welding models can also deviate from the DED process when considering the size (or thermal capacitance) of deposited surfaces. For instance, many welded surfaces are large

30

enough so that the deposition plane can be idealized as semi-infinite. In DED, however, tracks/volumes cannot be safely idealized as infinite and edge effects may need to be considered. A recent DED model, which employs the assumption of temperature-independent material properties, has been presented by Gockel et al. [54] in an effort to capture these edge effects. The authors solved the heat equation for a thin wall using the superposition of two-point heat sources symmetric about the edge of the wall. The solution to the melt pool geometry trended well with a finite element analysis (FEA) solution with temperature-dependent properties. Others have also formulated analytical models for various phenomena in DED such as clad geometry, beam attenuation, and powder heating that may be paired with other models for increased solution accuracy [55,56].

Convection heat transfer between the melt pool and the environment is another aspect often neglected in welding models. However, for DED modeling, the consideration of convection heat transfer can result in more accurate temperature field predictions. Heigel et al. [57] have shown that significant improvements in thermo-mechanical modeling can be achieved when employing spatially-varying heat transfer coefficients for convection modeling as opposed to only assuming uniform, free convection. Gouge et al. [58] compared numerical thermal results from when using free-convection-only to three different forced convection methods: uniform forced convection heat transfer coefficients from literature, forced convection coefficients obtained via lumped capacitance experiments, and forced convection coefficient values from hot-film anemometry measurements. It was shown that the hot-film anemometry based spatial convection coefficient values yielded the most accurate prediction of the part's temperatures. It was further shown that convection modeling should be applied to a continually-evolving mesh surface to capture the effects of material addition during DLD. Radiative heat transfer between

31

the melt pool and surroundings during DED, like convection, is often ignored in DED thermal modeling due to its non-linear complexity and it having minimal effect on bulk temperature predictions [59–61]. However, it has been shown to be significant in the melt pool and the surrounding heat affected zone (HAZ) due to its quartic temperature dependence [58].

Process maps (i.e. surface plots) have been developed from Rosenthal's analytical solution to aid DED process parameter selection for a variety of metallic materials [50,51]. Process maps are useful since they provide a means to estimate melt pool temperature, thermal gradients and cooling rates, as a function of dimensionless operating parameters. These estimated values are often used to study effects on melt pool geometry, residual stress, and microstructure of parts during DED. A limitation of Rosenthal-based process maps is that it can be difficult to incorporate detailed geometry effects since no precise knowledge of volume/boundary dimensions is accounted for.

3.2.2   DLD thermal monitoring

The final quality of DLD parts, as measured from their deviation from target properties and/or the existence of defects, not only varies with process parameters but also with the machine environment. The random nature of powder injection during the DLD process, as well as slight-to-large variations in powder quality, chamber conditions and more, contribute to machine-to-machine variability. *In situ* thermal monitoring can be used during AM [62] to better ensure repeatability; by matching thermal attributes related to a part's manufacture. While most AM processes allow for melt pool monitoring, DLD processes are unique in that 'bulk part' temperature distributions may also be monitored *in situ* due to the absence of a surrounding powder bed, e.g. in L-PBF. Such bulk temperature data can be used to estimate cooling rates in and around the HAZ of the part for determining material microstructures [35,36].

Early *in situ* inspections of the AM process utilized in-line cameras which collected electromagnetic radiation emitted by the melt pool to measure the dimensions of the melt pool [62,63]. These setups consisted of a camera and photodiode sensor directly in the optical path of the melt pool's perpendicular reflection to sufficiently capture local fluctuations with relatively high temporal and local resolution. A closed-loop feedback control system can then be used to stabilize the melt pool and keep the temperatures within a pre-defined window via knowledge of process mapping. Other thermal-based monitoring systems used for AM include high-speed cameras, infrared (IR) cameras and pyrometers. These systems have been used to monitor and study various AM phenomena such as 'balling', overheating, porosity generation, spatter generation, and powder consolidation. In general, the interpretation of IR thermometry can be challenging due to the rarity of high temperature, molten state emissivity data [64], which can be further complicated due to temperature and material dependence. These limitations can be obviated by using a dual-wavelength pyrometer by calibrating against the blackbody. However, the pyrometer can only measure the temperature variation within a small surface area such as the melt pool and cannot be used to measure the temperature of the entire part [65]. Seifi et al. [66] developed a new layer-wise process signature model using a dual-wavelength pyrometry and characterized defects in the part. A multi-sensor approach such as a combination of pyrometer and IR sensors to monitor melt pool and bulk part, respectively, provides an overall thermal monitoring solution [65,67]. Liu et al. [68] measured the brightness temperature of the melt pool by a pyrometer and gathered the data of the temperature gradient and cooling rate by IR imaging. Such imaging-based thermometry works best for thin-walled structures as the thermal distribution can be mostly considered two dimensional with temperatures approximately uniform in a direction that can be exposed to the imaging system.

33

The current work focuses on using thermographic images to help in creating and validating an analytical model for temperature within different-sized parts during DLD. Effects of part local thermal capacity (i.e. volume) on HAZ and melt pool thermal response are examined using both melt pool and bulk temperature images (dual thermography) obtained during the DLD of Ti-6Al-4V thin-walled structures. A validated, analytical means for determining how part size/geometry can impact local temperature, and thus, cooling rates and residual stress formation is presented. A low-fidelity, semi-analytical fin modeling approach, which provides for a more intuitive representation of the thermophysics while significantly reducing calculation time, is presented. The fin-modeled temperature distribution will be shown as a means for representing the temperature profile along the fabricated part.

3.3. Experimental setup & procedures

3.3.1 IR camera and pyrometer

Two thin-walled Ti-6Al-4V specimens of different lengths were fabricated with dimensions shown in Figure 12. The walls consisted of 60 successive, single tracks with thicknesses of approximately 2 mm. Wall length, a, was set to either 25.4 mm or 50.8 mm. An OPTOMEC LENS^{TM} 750 system with a Nd:YAG laser was employed for the fabrication of the thin walls using spherical, Plasma Rotating Electrode Process (PREP) Ti-6Al-4V powder (Phelly Materials, Inc). The size (diameter) distribution of the powder was between 44 μm and 149 μm. Parts were built on a non-heated Ti-6Al-4V substrate (153 x 153 x 3.3 mm^3) atop a CNC-controlled stage. Process parameters were determined through trial-and-error experimentation for yielding fully-dense, thick deposits. The major process parameters were found as: laser

output power = 290 W, a constant travel speed of 12.5 mm/s and a powder injection rate of 0.32 g/s.
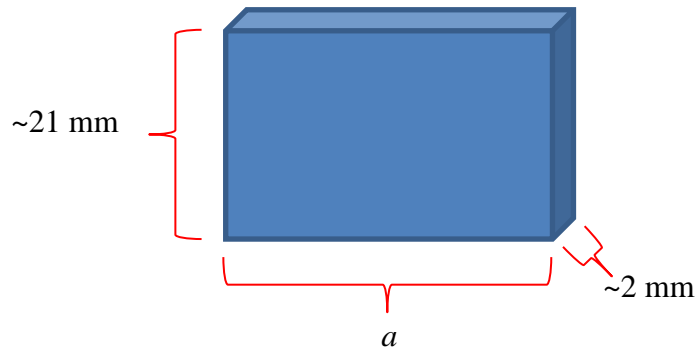
Figure 12. Dimensions of Ti-6Al-4V thin wall used for model validation experiments where *a* is either 25.4 mm or 50.8 mm.

An IR camera (Sierra-Olympic Technologies Inc., Viento320), which was mounted inside the LENS chamber to the build platform, gathered images of the temperature field along the surface of each thin wall. The IR camera possessed a spectral response range of 8–14 μm and was set to capture images at a rate of 14 Hz. Each camera pixel was found to correspond to a length of ~0.37 mm along each thin wall. A dual-wavelength pyrometer (Stratonics Inc.) was set up to view the melt pool (from above) and captured images at a rate between 4–7 Hz. The pyrometer was calibrated to black-body temperature prior to experimentation and did not require spectral adjustments [69]. For each image, all temperatures exceeding the liquidus temperature of Ti-6Al-4V were averaged together to determine the experimental, average melt pool temperature. More details regarding the IR camera and pyrometer setup, as well as actual thermographic data from experiments, are available in Ref. [65].

In order to properly calibrate the IR camera temperature scale for Ti-6Al-4V, the spectral, directional and temperature-dependent emissivity of the melt pool and HAZ must be known with

some level of certainty. It is difficult to find such properties of Ti-6Al-4V in the molten state

and at higher temperatures with spectral/directional dependence. Hence, IR data were linearly

scaled to dimensional temperature, T, using data from the dual-wavelength pyrometer (i.e. 'PM')

and ambient room temperature, T_∞, as shown in Eq. (1). The maximum steady-state temperature

value from pyrometer measurements was used to calibrate the maximum IR signal, whereas the

ambient room temperature was used to calibrate the lowest IR signal.

$$T(x) = T_\infty + \frac{IR(x) - IR_\infty}{IR_{max} - IR_\infty} \cdot PM_{max} \tag{1}$$

3.3.2   Analytical model

The DLD of the very first layer of Ti-6Al-4V atop a relatively large substrate can be

modeled as a non-accelerating moving heat source on a semi-infinite plane. During the

deposition of the first track, HAZ heat transfer is dominated by conduction (due to large volume

of the substrate) and thus the Rosenthal welding solution from the literature, Eq. (2) [3] can be

used for predicting temperature. Due to the asymptotic nature resulting from the point heat

source assumption, the temperature approaches infinity at the center of the laser beam. This

discontinuity can be avoided, and a finite maximum temperature achieved, when the heat source

is modeled as Gaussian distributed, as given in Eq. (3) [70]. Both solutions are plotted in Figure

13 as functions of position along the track when the laser source is at $x \cong 20$ mm along the thin

wall. The classical, exponential-decay temperature distribution trailing the deposition head may

be clearly seen. Note that Eq. (3) can still overestimate the melt pool temperature as it does not

account for convection, radiation, temperature-dependent thermal properties, and phase change

occurring within the melt pool. Although temperature-dependent properties are obtained from the

literature, thermophysical properties for the analytical solution are taken as a constant average

value at a temperature of 1000 K. The material properties are taken from Ref [24] for Ti-6Al-4V.

$$T(x,y,z,t) = T_\infty + \frac{Q}{2\pi k \sqrt{(x-Vt)^2 + y^2 + z^2}} e^{-\left(\frac{V}{2\alpha}\left(\sqrt{(x-Vt)^2 + y^2 + z^2} + (x-Vt)\right)\right)} \tag{2}$$

$$T(x,y,z,t) = T_\infty + \int_0^t \frac{Q}{\pi \rho c_p \sqrt{4\pi\alpha}} \cdot \frac{(t-\tau)^{0.5}}{2\alpha(t-\tau) + \sigma^2} e^{-\left(\frac{(x-V\tau)^2 + y^2\tau^2}{4\alpha(t-\tau) + 2R^2} + \frac{-z^2}{4\alpha(t-\tau)}\right)} d\tau \tag{3}$$
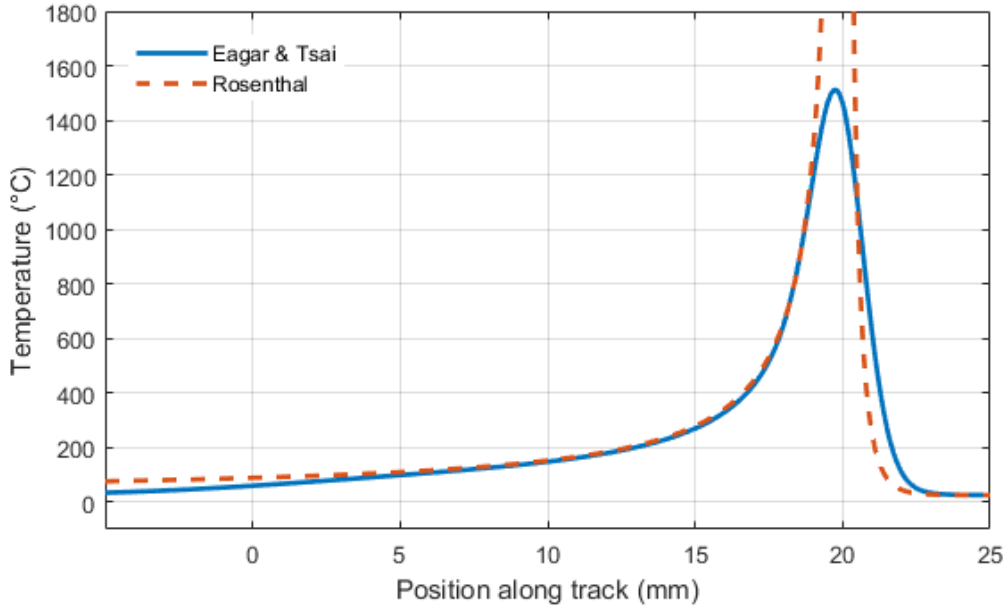
Figure 13: Temperature profile along first layer of Ti-6Al-4V on substrate along x-axis at y = 0 mm, z = 0 mm (t = 1.6 s) for DLD using analytical models from Rosenthal and Eagar & Tsai.

3.3.3 Numerical model

In order to validate analytical and experimental results, the FEA of the DLD of a Ti-6Al-4V thin wall was performed using COMSOL Multiphysics 5.4. The numerical simulation employed temperature-dependent material properties [24,71], as well as latent heating effects. Deposition modeling was carried out using the element activation method. An entire layer was added prior to laser scanning and activated once the laser beam of radius, R, reached within a

distance of $2R$ from the element. A volumetric Gaussian model, as shown in Eq. (4), was used to represent the laser heat source with a penetration depth equal to the layer thickness (l_t). The laser was deactivated once its position, denoted by (x_o, y_o), reached the end of the track, $(a, 0)$. The simulation then continued with a cooling phase (no heat source) to represent substrate/laser repositioning prior to the start of a new layer. A uniform heat transfer coefficient of $h = 1000$ W/m$^2\cdot$K is used to model the conduction through the relatively thick substrate which behaved as a heat sink during operation. A high value of the convection coefficient is assumed at the bottom of the substrate to allow for the heat sink behavior due to the presence of a copper spacer placed underneath the Ti-6Al-4V substrate during the experiment.

$$Q = \frac{A \cdot P}{2\pi R^2 l_t} \cdot e^{\left(-\frac{2\left((x-x_o)^2+(y-y_0)^2\right)}{R^2}\right)} e^{-\left(\frac{|z-z_0|}{l_t}\right)} \tag{4}$$

Forced convection between the part and shielding gas during DLD was modeled with a uniform heat transfer coefficient of $h = 60$ W/m$^2\cdot$K applied only within 15 mm of the laser source. A lower heat transfer coefficient of 25 W/m$^2\cdot$K was used for the remainder of the surface area. These values are within the range suggested by Ref [57] for forced convection in the LENS. A symmetry boundary condition was used along the direction of the track to reduce complexity and save computational time. The numerical model did not account for powder flow conditions and any melt pool thermo-capillary phenomenon. However, the solid-to-liquid phase change was tracked using COMSOL's built-in 'Phase Change Material' module, and material phase transition was set to occur when local temperatures were between the solidus and liquidus ($\Delta T_{1\rightarrow2}$). The amount of material in each phase is tracked using variable, θ, for each phase. The phase change transition can be represented in Figure 14 [72]. Radiation losses were accounted for using a total surface-to-ambient emissivity ($\varepsilon = 0.75$) for Ti-6Al-4V.
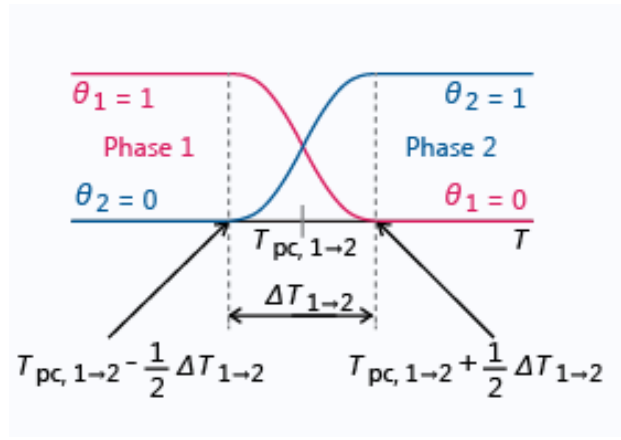
Figure 14: Transition of properties during phase change with temperature [72]
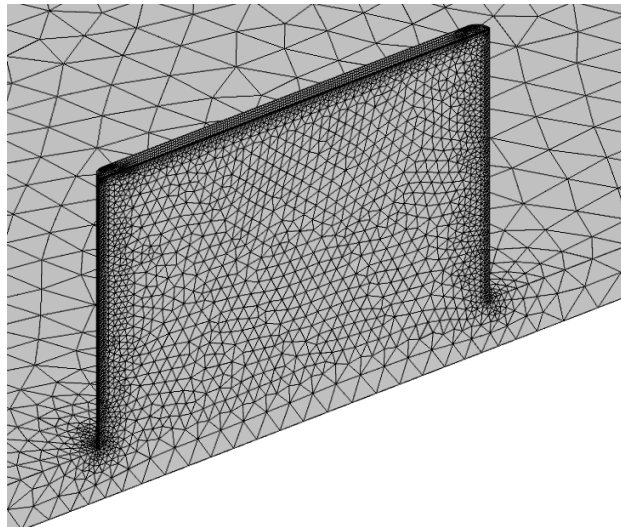
Figure 15: Mesh used in modeling of DLD process showing finer elements on the top layer for Layer 50

An appropriate non-uniform tetrahedral mesh was selected based on the mesh independence study performed on the cladding of the first layer. The mesh consisted of finer elements in the laser track region, as shown in Figure 15, and inflates in size towards the substrate. The mesh is auto-updated to reflect material addition for each new layer. The result from the previous solution is then applied as an initial condition for the new domain. Non-initialized nodes, e.g. nodes within the new layer, are set to be initialized with the ambient

temperature values. A time-adaptive stepping method provided by COMSOL Multiphysics 5.4, as described in Chapter 2.3, was used to ensure time-independent solutions. Results from the single-track multi-layer numerical simulation of the thin wall are later compared against the thermal data obtained from performed experiments. Numerical simulation of 50 consecutive thin-wall tracks took approximately 72 hours using 20 processors. Temperature results from the numerical model hold similar errors and uncertainty as mentioned in Chapter 2.3, arising from spatially varying, temperature-dependent spectral properties of the material. Inaccuracies in the experimental temperature values can be partially attributed to instantaneous dynamics (powder spatter, plume formation), as well as the assumption of a linear scale in the IR calibration.

3.4.   Results and discussion

3.4.1   Thermography: General findings

Thermographic images depicting the melt pool and HAZ during the DLD of select layers of the 25-mm and 50-mm thin walls are displayed in Figure 16. Underneath each IR camera image in Figure 16 is a representative, corresponding melt pool (pyrometer) image at a similar point in time. Note that raw IR images are presented on the pyrometer-calibrated temperature scale (Eq. (1)). The scale in the middle of the figure applies to the pyrometer images and describes their temperatures in °C.
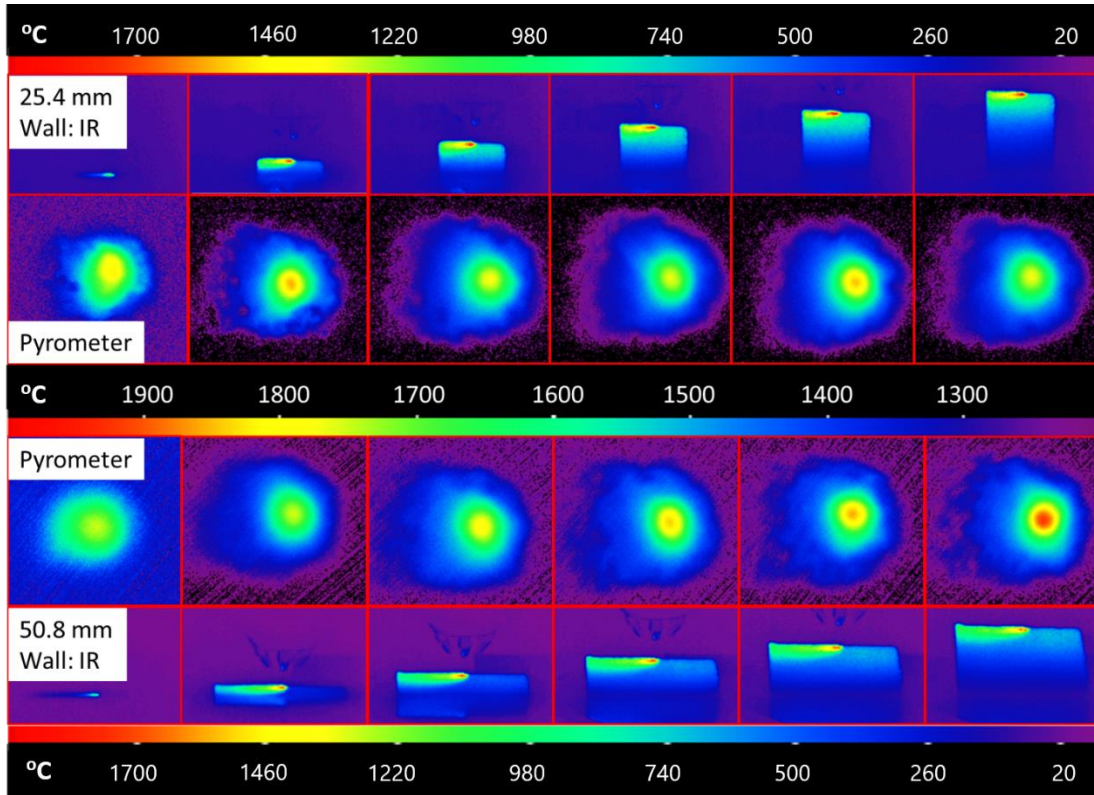
Figure 16: Layer-by-layer evolution of IR-camera-measured temperature profile for 25-mm (top) and 50-mm (bottom) thin walls. The middle scale relates only to the pyrometer images while the top and bottom scales relate to IR images. The IR temperature scales are post-calibrated using Eq. 1. Images left to right depict Layers 1, 10, 21, 34, 45, & 60.

From Figure 16, it may be seen that the Ti-6Al-4V melt pool consists of peak temperatures are around 1900 °C. In general, the 50-mm thin wall consisted of melt pools with higher peak temperatures, especially at later layer numbers. As shown in Figure 16, the bulk temperature of the 25-mm thin wall is generally higher than that for the 50-mm thin wall due to its heat retention. The pyrometer results show that the melt pool size of the 25-mm wall is slightly larger as compared to the 50-mm wall, which can be attributed to the higher bulk heat retention as well as lower layer clad duration in the 25-mm thin wall. It can also be observed that the melt pool size in the 25-mm continues to grow until layer-21, whereas the observed size in

the 50-mm is quite uniform starting layer-10. A higher value of peak melt pool temperature in the 60th layer of the 50-mm thin wall can be observed, which is an outlier during the experiment and may have occurred due to higher temperature value resulting from instantaneous spatter dynamics. A normalized peak temperature curve during the entire process showed no such peculiarity.

3.4.2 Melt pool temperature

As shown in Figure 17, the peak melt pool temperatures near 1975 ºC were measured initially during the DLD of the 25-mm thin wall, while the peak temperatures never exceed 1860 ºC for the longer wall, and unlike the 25-mm thin wall, the higher peak temperatures were observed to occur at later layers. It can be observed that the average melt pool temperatures for both thin walls stay between 1700 ºC – 1750 ºC. The maximum melt pool temperature for the 25-mm thin wall has a wider range relative to the 50-mm thin wall, with higher values existing during initial layer deposits. An evolutionary melt pool temperature, which depends on layer number and part size, appears to exist. From Figure 17, it may be seen that the 25-mm wall's melt pool temperature initially overshoots its steady-state average, and less time is required to achieve a melt pool that becomes near-independent of layer number, i.e. steady state. Kledwig et al. [73] observed similar overshooting behavior in the first 200 s of the experiment and attributed this transiency to the heat-up dynamics in the camera. The monitoring was conducted using a CCD camera-based temperature measuring system that worked at 740 nm wavelength. A numerical solution, as shown in Figure 18, revealed that no such phenomenon occurs solely due to part size effects. Numerical results line up more closely with the IR signal data than that from pyrometer. For a constant scan speed of ~12.5 mm/s and a reposition speed of ~25 mm/s, the 25-

mm thin wall allowed for approximately 2 s of in-process time and 2.75 s of post-build time interval (dwell time) between each layers compared to 4 s of in-process time and 3.6 s of post-layer time interval in the 50-mm long wall.
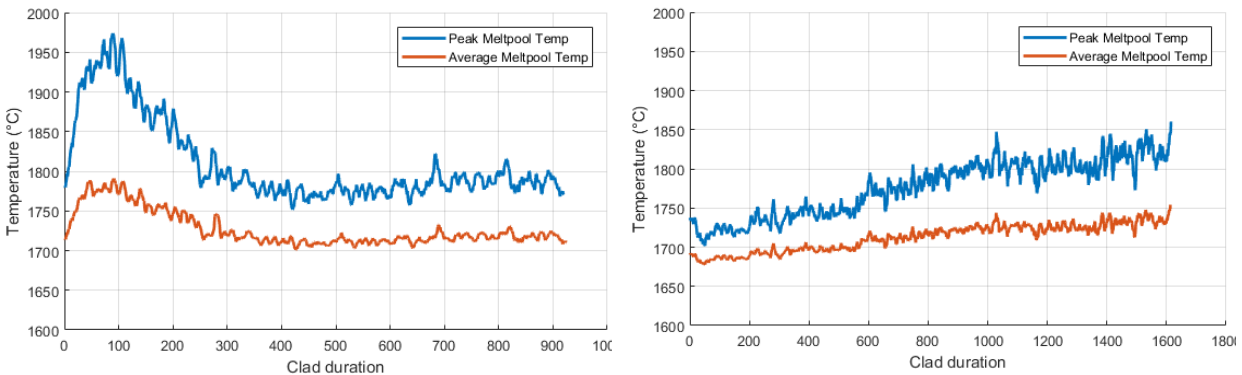
Figure 17: Maximum and average melt pool temperatures in 25-mm (left) and 50-mm (right) thin walls during the active duration of the build measured using a dual-wavelength pyrometer

It may be seen that, from Figure 17, the average melt pool temperature reaches 1800 ℃ during the layer-wise overshoot of the 25-mm wall, whereas it falls to just above the melting point temperature of 1660 ℃. The melt pool temperature of the 50-mm wall, however, can be seen to increase with the number of deposited layers linearly before reaching steady melt pool temperatures. The suppression of the overshoot may be the result of an increased time interval between layers for higher heat dissipation, which allows for a quasi-steady-state condition within the fabricated part. For the number of layers examined, both the maximum and the average melt pool temperatures are found to be increasing with the build-height until steady-state. In both cases, the melt pool temperatures were found to achieve steady-state values after deposition of ~20-30 layers. This can be attributed to three major factors: a) edge effects from semi-infinite

43

substrate b) delay due to latent heat effect, and c) residual heat build-up from previous laser scanning.

The initial laser interaction occurs on a flat substrate at room temperature. As a result, the maximum temperature achieved may be very less even in ideal situations. However, during subsequent passes, the laser interaction occurs on a cladded solid which is at a temperature much higher than the room temperature. Therefore, the maximum melt pool temperature rises with an increasing number of passes until further resistances incur on the melt pool. Another important resistance besides latent heat is the radiation loss which plays an important role in stabilizing the maximum temperature within the melt pool. Note that, in both cases, by the end of 60 layers, the maximum melt pool temperature and average melt pool temperature becomes steady around 1800 ℃ and 1725 ℃, respectively. This suggests that for thin walls the steady-state maximum melt pool temperature may not be a function of time interval or part size. However, the time or the number of layers required to get to this steady-state thermal profile may vary by the size of the thin wall. In the experiment performed, the steady-state thermal history was achieved approximately at Layer 21 for the 25-mm wall as compared to Layer 40 for the 50-mm. Numerical simulations were stopped after 50 layers for both cases since no significant changes were found.

It may be observed from both the experimental as well as numerical studies (Figure 18) that the 50-mm wall provides a slightly lower initial preheat for the subsequent laser pass as compared to the 25-mm wall. This agrees with the fact that the 50-mm wall offers more time for cooling and thermal diffusion. The disagreement between the numerical and experimental results during the first few layers of both thin walls can be attributed to the reduced absorptivity in the initial layers due to poor surface-laser interaction. While, it can be observed from the
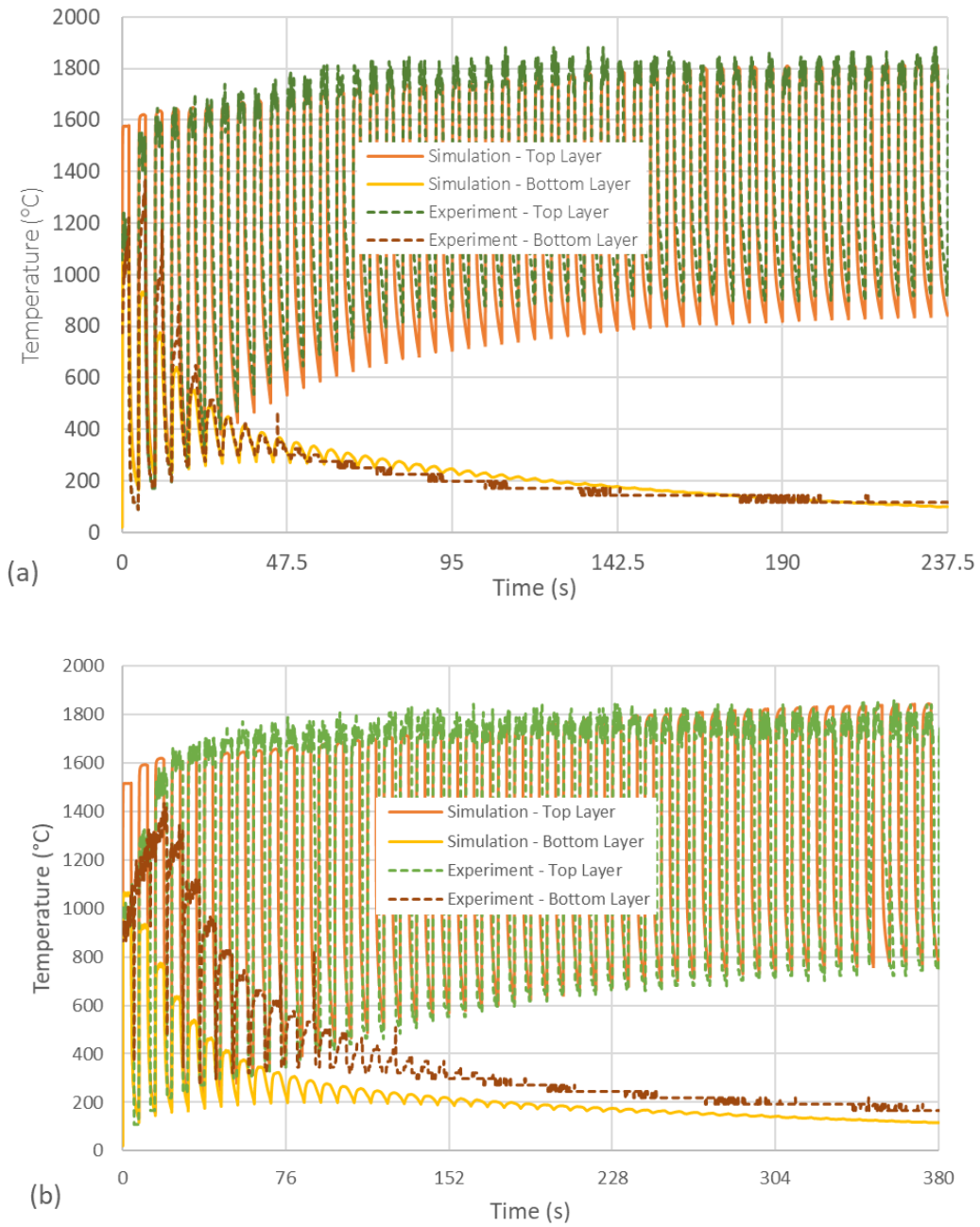
Figure 18: Experimental and numerical comparison of maximum temperature values with time at the top and bottom layers of (a) 25-mm and (b) 50-mm walls.

experimental results that the 50-mm wall stores more heat energy per unit volume than predicted by the numerical results resulting in higher temperature values at the substrate, this may arise

45

from the uncertainty associated with the temperature-dependent material properties taken from the literature.

It has been observed by [74] that smaller perturbations in the boundary conditions during the AM process such as incident power and the heat transfer coefficient within the melt pool play a small role in affecting its temperature profile. This can be seen from the scatter in both the IR signal and the pyrometer readings of the temperature values. Although some fraction of these scatters may be related to instrumentation error, the remaining may be contributed to the dynamic powder, melt pool, and laser interaction. Nevertheless, the temperature values outside the melt pool were found to be scatter-less. This is because most of the deposited energy from the laser is diffused by conduction through the part and the substrate. However, thin-walled parts such as fins and lattices provide minimal area for conductive heat transfer to the substrate. In other words, for the same number of layers conductive thermal resistance (R_{th}) is higher for smaller geometries as evidenced by equation $R_{th} = L/(kA_c)$, where, k, L and A_c are the thermal conductivity, characteristic length and cross-sectional area of the deposited part, respectively. This results in slower cooling rates and reduced thermal gradients. In extreme cases, unwanted outcomes such as localized vaporization and evaporation of the melt may prevail resulting in more frequent spatters during the process.
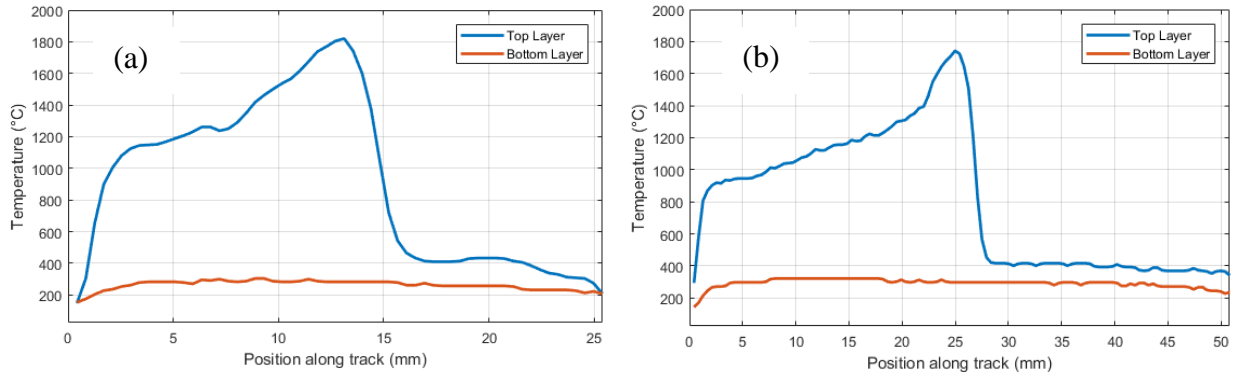
Figure 19: Normalized IR temperature from the top (blue) and bottom (red) layers of a) 25-mm and b) 50-mm wall. The bottom layer shows approximately uniform temperature starting at Layer 11 and Layer 18, respectively.

3.4.3 Substrate affected zone

As the build height increases during DLD, the convection heat transfer from the structure, especially for thin-walled parts, increases due to there being more surface area. Due to convection, the temperature at the substrate and lower layers of the fabricated part approaches ambient temperature. This region of the part does not have a significant temperature response during the DLD of the top-most layer and can be defined as the "Substrate Affected Zone" (or SAZ). Figure 19 shows the temperature from the IR at the active build layer and the substrate/part interface during SAZ onset. The height of SAZ increases with build height as the distance between the substrate and the HAZ increases. The SAZ effects were seen within the first 11 layers in the 25-mm wide wall, compared to 18 layers in the 50-mm wide wall. It should also be noted that on the onset of SAZ, the temperature variation within the layer is minimal further emphasizing the observation that the SAZ does not see the effect of moving heat source.

The number of layers (or the height of the part) until the SAZ appears can be predicted using the relation proposed below in Eq. 5. While the broadness of the current relationship has

47

not been tested, it has been found to accurately predict for thin wall experiments performed by

the authors at multiple layers during the build process. The relationship is derived from the

Fourier number ($Fo = \frac{t\,\alpha}{L_c^2}$) but accommodated to allow for the laser position, deposition-head

repositioning time (t_{repos}) and the extraneous dwell time (t_{dwell}) spent after each layer. The

significance of this value is that solid part after this height (L_c) will have a similar thermal

history. This can also be used to calculate the edge/substrate effects due to the moving heat

source. For example, the initial part of the deposited clad (of thickness equal to the characteristic

length), as well as the volume deposited at the end (equal thickness to the characteristic length)

will have a dissimilar history as compared to the middle portion of the build.

$$L_c \cong \sqrt{\left(t_{dwell} + t_{repos} + \frac{x_0}{V}\right)\alpha} \qquad (5)$$

The calculation of SAZ onset height allows for the separation of regions within the part

being fabricated into two zones: a transient (evolving) and the steady-state region as shown in

Figure 20. The temperature distribution in the latter region can then be approximated using a

one-dimensional fin model since the moving heat source no-longer affects this region.
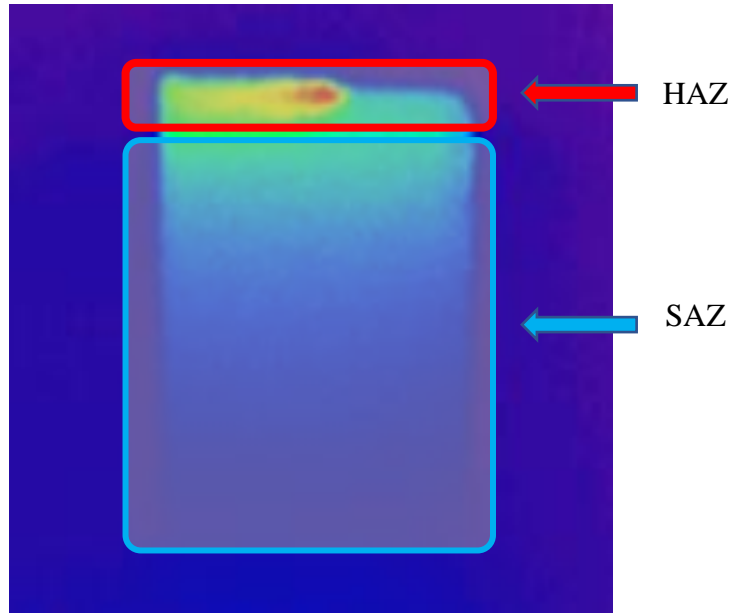
Figure 20: IR temperature distribution of thin wall showing HAZ (transient region modeled with thermal spreading) and SAZ (quasi-steady state) region for the fin modeling approach

3.5.   Fin analogy

In order to estimate temperature variation along a thin wall during DLD, a fin analogy is utilized. This approximation holds true particularly in the SAZ region of thin walls where the temperature variation within a layer is minimal and dominant changes occur in the height-wise direction. The temperature at the top-most layer of the SAZ region can be taken as the base temperature for a rectangular fin. The HAZ region can then be treated as a steady, uniform heat flux at the SAZ boundary. The temperature distribution in the thin wall with the convective tip condition, with coefficient h_{tip}, is given by Eq. (6) [75]. The terms Θ, Θ_b represent temperature in the fin, and base, respectively, whereas m is the fin parameter, which is given by $m = \sqrt{\frac{hP}{kA_c}}$.

The wall/substrate interface is idealized as a fin tip with uniform heat transfer coefficient found via Eq. (7).

$$\Theta = \Theta_b \left(\frac{\cosh m(L-x) + \frac{h_{tip}}{mk} \sinh m(L-x)}{\cosh mL + \frac{h_{tip}}{mk} \sinh mL} \right) \tag{6}$$

$$h_{\text{tip}} = \frac{k_{\text{subs}}}{l_{\text{subs}}}, \tag{7}$$

where k_{subs} and l_{subs} are the thermal conductivity and thickness of the substrate, respectively.

The energy absorbed by the injected powder was obtained using the model proposed by Pinkerton et al. [56]. After compensating for convective and radiative losses from the melt pool, the energy conducted through the melt pool (P_{cond}) was found to be approximately 40% of incident laser power and this is consistent with other observations in the literature. Since the DLD process involves the repositioning and idling of the deposition head (with laser off) prior to depositing a new track, a time-averaged method has been proposed to calculate the energy dissipation by the thin wall, given by Eq. (8).

$$P_{\text{fin}} = P_{\text{cond}} \cdot \frac{t_{\text{active}}}{t_{\text{active}} + t_{\text{dwell}} + t_{\text{repos}}} \tag{8}$$

The temperature difference between the liquidus and the beginning of the SAZ can be predicted using a thermal spreading resistance approach. For this study, the thermal spreading resistance model proposed by Muzychka and Yovanavich [76] for a circular moving heat source is used and presented in Eq. (9). The proposed model relates spreading resistance (R_{sp}) to the Peclet number (Pe), which may be interpreted as a measure of thermal penetration. It was derived that as the Pe approaches infinity, thermal penetration approaches a zero value. Constant thermal conductivity (k) is used by the fin model and is based on average values over the range of temperatures in the SAZ region. A key challenge in using the model is the prediction and use

of an average heat transfer convection coefficient along the sides/faces of the walls, $\bar{h}$. The average convection coefficient for the wall is obtained by integrating the spatial relation proposed by Heigel et al [57] over the area of the wall. The higher heat transfer coefficient of the smaller wall may be a result of wall size being nearly equal to the nozzle's forced convection region. As a result, the forced convective value weighed in more for the smaller thin wall. Consequently, the natural convection values were found to be dominant for larger sizes as demonstrated by Heigel et. al [56].

$$R_{sp} = \frac{1}{k \cdot R} \cdot \frac{0.323}{\sqrt{Pe}} \tag{9}$$

$$Pe = \frac{V \, d_{mp}}{\alpha} \tag{10}$$

To obtain an average layer temperature from IR images, each row of pixels extending from edge to edge of the melt pool (~5 pixels wide) was averaged together from the top of the wall to the bottom as shown in Figure 21. Average temperature distribution along the height of the walls was compared against the results from the proposed fin model, the results of which are shown in Figure 22.
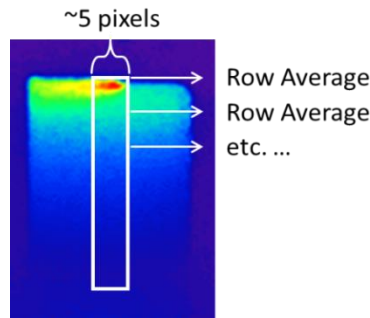
Figure 21: Example of pixel averaging method used to evaluate temperature data along the height of a thin wall for fin analysis

It may be observed that the proposed fin model works well in predicting the temperature distribution along the SAZ region. Additionally, for both sizes, the heat dissipation from the fin model agrees within 5% of the power pumped by the HAZ as calculated by Eq. (7). For the 50-mm thin wall, a lower convection coefficient resulted in a more linear looking temperature distribution along the wall as compared to the 25-mm wall. As a result, a hyperbolic temperature profile was observed for the smaller wall. Both the experimental data and the proposed fin model suggest a slight increase in the substrate's temperature on the 50-mm thin wall. This can be attributed to a higher time-averaged effective heat flux obtained due to reduced dwell time as compared to the active laser duration.

(a)

(b)

(c)
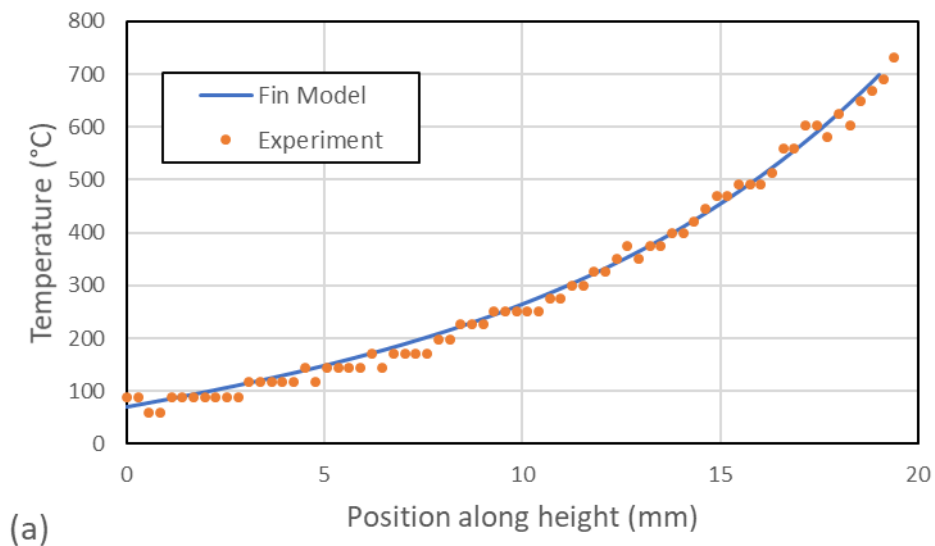
Figure 22: Temperature profile along height in (a) 25-mm, (b) 50-mm, and (c) 39.3 mm thin wall from literature

As a secondary validation, the fin-model is applied to data taken from literature from Ref. [57] with no dwell case. The temperature distribution within the S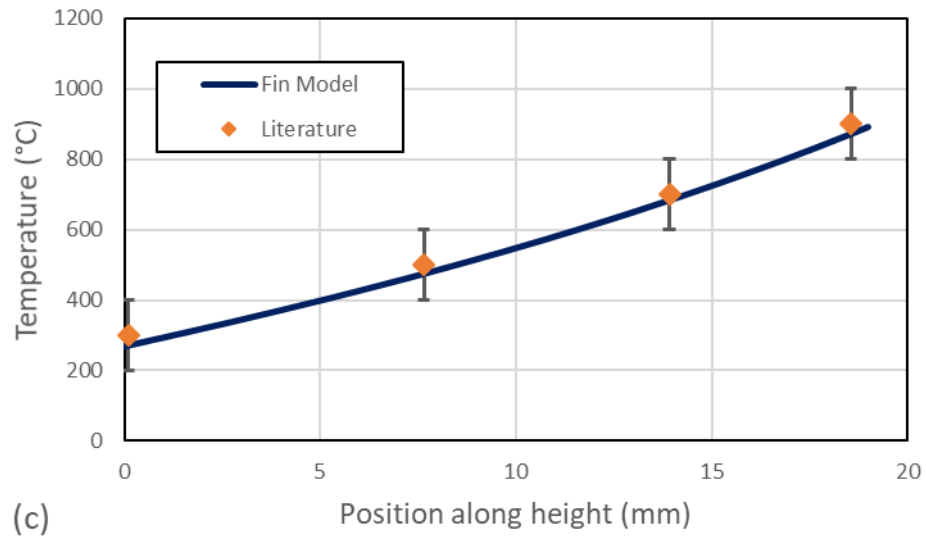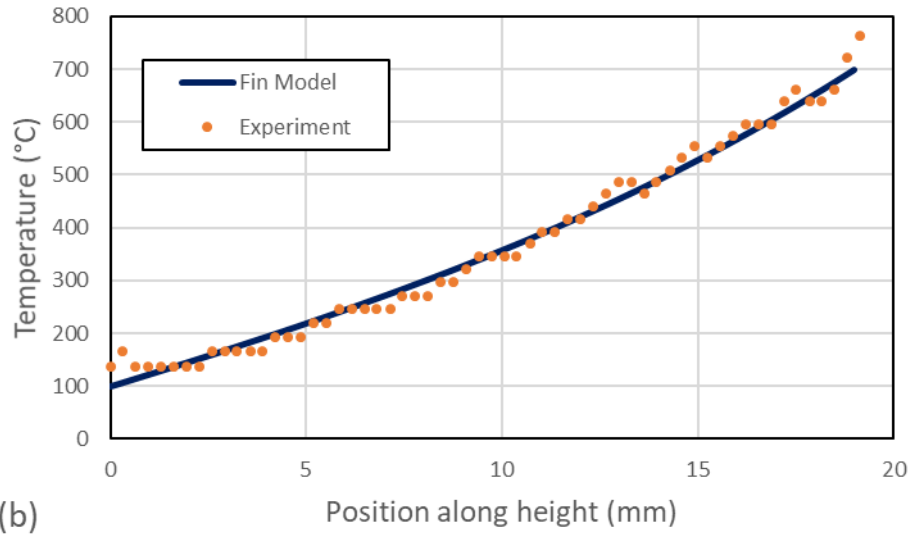AZ is shown in Figure 22(c). Error bars are included within the plot to represent uncertainty in data extraction due to lower

53

contour resolution. It was observed that the temperature trend within the profile agrees quite well with that proposed by the fin model. Additionally, in an inverse technique, the proposed model can also be used in conjunction with an in-built thermocouple at the substrate to obtain the temperature profile through the thin-wall as a function of wall height. Unlike numerical methods, the proposed analytical method takes a simplistic approach to speed up rapid calculation of temperature distribution within the bulk region of the fabricated part within seconds. However, further work is necessary to validate such results.

3.6.   Conclusions

The effects of part size on its temperature distribution during the DED process were investigated through dual-thermographic monitoring and a unique modeling technique for predicting size effects on temperature was presented. Based on the results, the following conclusions can be made:

1. The duration of dwell times presented to be a major contributing factor affecting the rate at which the thermal steady-state is achieved. As a result, the longer wall took significantly more layers/time to achieve a uniform temperature profile within the wall.

2. Maximum and average melt pool temperatures appear to be near independent of part size at steady-state. Finite element simulation results showed that a quasi-steady melt pool temperature may be unique to a layer especially during an earlier cladding process near the substrate and that the layer-wise steady melt pool was achieved within the first few seconds of track scanning.

3. The proposed fin modeling-based temperature distribution was found to accurately predict the thermal profile in the SAZ along the scan direction within 15%. A method to predict the onset of SAZ has also been proposed.

The work presented herein can aid in filling the void in the AM industry, by providing the ability to understand bulk heating effects during multi-pass DED. The current work provides a step in the ability to estimate initially used process parameters that would be required to engineer the built material. With more research, the model may have in situ applications for controlling thermal history when paired with monitoring technology. While the proposed model does not serve as a replacement to transient finite analyses, it can also be used in conjunction with the FEA to consolidate a larger SAZ zone as a fin with prescribed temperature and gradients. The expansion and applicability of the consolidation model will be presented in future work.

3.7. Acknowledgments

Chapter 4: Conclusions and Future Work

Numerical simulation of two different types of metal-based AM processes was performed with augmented physical modeling. Through numerical analyses, the effects of the overhang angle on the morphology of the melt pool were studied during the L-PBF process. Similarly, the effects of geometry size during the DLD of a thin wall was also investigated. The results were compared against data from an IR camera for validation and further analyses. It was noted that the computational time to simulate the AM processes was impractical. Consequently, a low-fidelity, fin model was proposed for the fast-prediction of thermal history within the bulk of the deposited clad. The model fared within 15% of the experimental results while saving significant amount of computational time. The following conclusions were drawn from the process effects studies:

1. The melt pool depth was found to be very sensitive to the overhang angle as compared to the melt pool width and peak temperature (L-PBF).

2. For the materials and angles investigated, for overhang angles less than 30°, change in melt pool dimensions was insignificant (L-PBF).

3. The 50-mm wall took a longer time to reach a steady thermal history as compared to 25-mm wall (DLD).

4. For the number of layers studied, the melt pool temperatures of the 25-mm wall remained at higher values than the 50-mm wall (DLD). Contrarily, the substrate temperatures of the 25-mm wall were found to be at lower values than the 50-mm wall deposition.

5. The substrate was found to affect the thermal build-up within the first one-third of the deposition process studied before the part geometry size itself dictate the heat flow rate.

The current work focused on predicting the bulk thermal data of the deposited clad using the analytical fin-model. More work is necessary to expand the model in applications other than thin geometries. Additionally, further research is required to couple the bulk temperature prediction to the localized HAZ thermal distribution.

Considering the work in this research, it can be suggested that overhang angles in excess of 30° may be detrimental to the accuracy of material properties as well as the dimensionality of the fabricated part, and should be avoided when possible. It was shown that beyond this angle, careful consideration should be made as the melt pool morphology may be very sensitive to the powder feedstock itself. While monitoring tools such as IR are quite helpful in tracking thermal history, accurate temperature prediction is still a topic of research. The proposed model may serve as a tool to predict the bulk temperature of the part in the absence of expensive monitoring tools. Additionally, a cheap thermocouple at the substrate can be coupled with the fin-model to accurately model the bulk temperature history of the entire SAZ.

References

[1] M. Masoomi, S.M. Thompson, N. Shamsaei, Laser powder bed fusion of Ti-6Al-4V parts: Thermal modeling and mechanical implications, International Journal of Machine Tools and Manufacture. 118–119 (2017) 73–90. https://doi.org/10.1016/j.ijmachtools.2017.04.007.

[2] S.M. Thompson, L. Bian, N. Shamsaei, A. Yadollahi, An overview of Direct Laser Deposition for additive manufacturing; Part I: Transport phenomena, modeling and diagnostics, Additive Manufacturing. 8 (2015) 36–62. https://doi.org/10/gd7gqw.

[3] D. Rosenthal, The Theory of Moving Sources of Heat and Its Application to Metal Treatments, Trans. A.S.M.E. (1946) 849–866.

[4] A. Vasinonta, J.L. Beuth, M.L. Griffith, A Process Map for Consistent Build Conditions in the Solid Freeform Fabrication of Thin-Walled Structures, J. Manuf. Sci. Eng. 123 (2001) 615. https://doi.org/10.1115/1.1370497.

[5] A. Vasinonta, J.L. Beuth, M. Griffith, Process Maps for Predicting Residual Stress and Melt Pool Size in the Laser-Based Fabrication of Thin-Walled Structures, J. Manuf. Sci. Eng. 129 (2007) 101. https://doi.org/10/ft58cv.

[6] A.M. Rubenchik, W.E. King, S.S. Wu, Scaling laws for the additive manufacturing, Journal of Materials Processing Technology. 257 (2018) 234–243. https://doi.org/10.1016/j.jmatprotec.2018.02.034.

[7] H. Peng, M. Ghasri-Khouzani, S. Gong, R. Attardo, P. Ostiguy, B.A. Gatrell, J. Budzinski, C. Tomonto, J. Neidig, M.R. Shankar, R. Billo, D.B. Go, D. Hoelzle, Fast prediction of thermal distortion in metal powder bed fusion additive manufacturing: Part 1, a thermal circuit network model, Additive Manufacturing. 22 (2018) 852–868. https://doi.org/10/gf3jzm.

[8] M.P. Mughal, H. Fawad, R. Mufti, Finite element prediction of thermal stresses and deformations in layered manufacturing of metallic parts, Acta Mechanica. 183 (2006) 61–79. https://doi.org/10/dkwn4b.

[9] R. Andreotta, L. Ladani, W. Brindley, Finite element simulation of laser additive melting and solidification of Inconel 718 with experimentally tested thermal properties, Finite Elements in Analysis and Design. 135 (2017) 36–43. https://doi.org/10.1016/j.finel.2017.07.002.

[10] T. Keller, G. Lindwall, S. Ghosh, L. Ma, B.M. Lane, F. Zhang, U.R. Kattner, E.A. Lass, J.C. Heigel, Y. Idell, M.E. Williams, A.J. Allen, J.E. Guyer, L.E. Levine, Application of Finite Element, Phase-field, and CALPHAD-based Methods to Additive Manufacturing of Ni-based Superalloys, Acta Materialia. 139 (2017) 244–253. https://doi.org/10.1016/j.actamat.2017.05.003.

[11] V. Ankudinov, G.A. Gordeev, M.D. Krivilyov, Numerical simulation of heat transfer and melting of Fe-based powders in SLM processing, IOP Conf. Ser.: Mater. Sci. Eng. 192 (2017) 012026. https://doi.org/10.1088/1757-899X/192/1/012026.

[12]   W. Sudnik, D. Radaj, S. Breitschwerdt, W. Erofeew, Numerical simulation of weld pool geometry in laser beam welding, J. Phys. D: Appl. Phys. 33 (2000) 662–671. https://doi.org/10.1088/0022-3727/33/6/312.

[13]   W.J. Sames, F.A. List, S. Pannala, R.R. Dehoff, S.S. Babu, The metallurgy and processing science of metal additive manufacturing, International Materials Reviews. 61 (2016) 315–360. https://doi.org/10.1080/09506608.2015.1116649.

[14]   M.J. Matthews, G. Guss, S.A. Khairallah, A.M. Rubenchik, P.J. Depond, W.E. King, Denudation of metal powder layers in laser powder bed fusion processes, Acta Materialia. 114 (2016) 33–42. https://doi.org/10.1016/j.actamat.2016.05.017.

[15]   S. Shrestha, S. Rauniyar, K. Chou, Thermo-Fluid Modeling of Selective Laser Melting: Single-Track Formation Incorporating Metallic Powder, J. of Materi Eng and Perform. 28 (2019) 611–619. https://doi.org/10/gf3jxw.

[16]   N. Makoana, I. Yadroitsava, H. Möller, I. Yadroitsev, Characterization of 17-4PH Single Tracks Produced at Different Parametric Conditions towards Increased Productivity of LPBF Systems—The Effect of Laser Power and Spot Size Upscaling, Metals. 8 (2018) 475. https://doi.org/10/gfbm34.

[17]   M. Masoomi, J.W. Pegues, S.M. Thompson, N. Shamsaei, A numerical and experimental investigation of convective heat transfer during laser-powder bed fusion, Additive Manufacturing. 22 (2018) 729–745. https://doi.org/10/gf3jx4.

[18]   P. Hartunian, M. Eshraghi, Effect of Build Orientation on the Microstructure and Mechanical Properties of Selective Laser-Melted Ti-6Al-4V Alloy, JMMP. 2 (2018) 69. https://doi.org/10.3390/jmmp2040069.

[19]   A. Ataee, Y. Li, D. Fraser, G. Song, C. Wen, Anisotropic Ti-6Al-4V gyroid scaffolds manufactured by electron beam melting (EBM) for bone implant applications, Materials & Design. 137 (2018) 345–354. https://doi.org/10/gctnxs.

[20]   A. Yadollahi, N. Shamsaei, S.M. Thompson, A. Elwany, L. Bian, Effects of building orientation and heat treatment on fatigue behavior of selective laser melted 17-4 PH stainless steel, International Journal of Fatigue. 94 (2017) 218–235. https://doi.org/10.1016/j.ijfatigue.2016.03.014.

[21]   M. Simonelli, Y.Y. Tse, C. Tuck, Effect of the build orientation on the mechanical properties and fracture modes of SLM Ti–6Al–4V, Materials Science and Engineering: A. 616 (2014) 1–11. https://doi.org/10.1016/j.msea.2014.07.086.

[22]   J.C. Fox, S.P. Moylan, B.M. Lane, Effect of Process Parameters on the Surface Roughness of Overhanging Structures in Laser Powder Bed Fusion Additive Manufacturing, Procedia CIRP. 45 (2016) 131–134. https://doi.org/10.1016/j.procir.2016.02.347.

[23]   J.J. Valencia, P.N. Quested, Thermophysical Properties, (2008) 468–481. https://doi.org/10.1361/asmhba0005240.

[24] M. Boivineau, C. Cagran, D. Doytier, V. Eyraud, M.-H. Nadal, B. Wilthan, G. Pottlacher, Thermophysical Properties of Solid and Liquid Ti-6Al-4V (TA6V) Alloy, Int J Thermophys. 27 (2006) 507–529. https://doi.org/10/b2fwt2.

[25] C. Tang, J.L. Tan, C.H. Wong, A numerical investigation on the physical mechanisms of single track defects in selective laser melting, International Journal of Heat and Mass Transfer. 126 (2018) 957–968. https://doi.org/10/gf3jx6.

[26] S. Ghosh, L. Ma, L.E. Levine, R.E. Ricker, M.R. Stoudt, J.C. Heigel, J.E. Guyer, Single-Track Melt-Pool Measurements and Microstructures in Inconel 625, JOM. 70 (2018) 1011–1016. https://doi.org/10.1007/s11837-018-2771-x.

[27] S.S. Sih, J.W. Barlow, The Prediction of the Emissivity and Thermal Conductivity of Powder Beds, Particulate Science and Technology. 22 (2004) 427–440. https://doi.org/10.1080/02726350490501682.

[28] M.R. Alkahari, T. Furumoto, T. Ueda, A. Hosokawa, R. Tanaka, M.S. Abdul Aziz, Thermal Conductivity of Metal Powder and Consolidated Material Fabricated via Selective Laser Melting, KEM. 523–524 (2012) 244–249. https://doi.org/10/gf3jzg.

[29] L.C. Wei, L.E. Ehrlich, M.J. Powell-Palm, C. Montgomery, J. Beuth, J.A. Malen, Thermal conductivity of metal powders for powder bed additive manufacturing, Additive Manufacturing. 21 (2018) 201–208. https://doi.org/10/gf3jzw.

[30] E.R. Denlinger, V. Jagdale, G.V. Srinivasan, T. El-Wardany, P. Michaleris, Thermal modeling of Inconel 718 processed with powder bed fusion and experimental validation using in situ measurements, Additive Manufacturing. 11 (2016) 7–15. https://doi.org/10.1016/j.addma.2016.03.003.

[31] C.D. Boley, S.C. Mitchell, A.M. Rubenchik, S.S.Q. Wu, Metal powder absorptivity: modeling and experiment, Appl. Opt. 55 (2016) 6496. https://doi.org/10.1364/AO.55.006496.

[32] M.L. Griffith, M.E. Schlienger, L.D. Harwell, M.S. Oliver, M.D. Baldwin, M.T. Ensz, M. Essien, J. Brooks, C.V. Robino, J.E. Smugeresky, W.H. Hofmeister, M.J. Wert, D.V. Nelson, Understanding thermal behavior in the LENS process, Materials & Design. 20 (1999) 107–113. https://doi.org/10.1016/S0261-3069(99)00016-3.

[33] M.L. Griffith, D.M. Keicher, C.L. Atwood, J.A. Romero, J.E. Smugeresky, L.D. Harwell, D.L. Greene, Free Form Fabrication of Metallic Components Using Laser Engineered Net Shaping (Lens), in: 1996. https://doi.org/10.15781/T26689430.

[34] S. Bontha, N. Klingbeil, Thermal Process Maps for Controlling Microstructure in Laser-Based Solid Freeform Fabrication, in: Austin, TX, 2003: pp. 219–226.

[35] A.R. Nassar, J.S. Keist, E.W. Reutzel, T.J. Spurgeon, Intra-layer closed-loop control of build plan during directed energy additive manufacturing of Ti–6Al–4V, Additive Manufacturing. 6 (2015) 39–52. https://doi.org/10.1016/j.addma.2015.03.005.

[36] C. Qiu, G.A. Ravi, M.M. Attallah, Microstructural control during direct laser deposition of a β-titanium alloy, Materials & Design. 81 (2015) 21–30. https://doi.org/10.1016/j.matdes.2015.05.031.

[37]   A.J. Sterling, B. Torries, N. Shamsaei, S.M. Thompson, D.W. Seely, Fatigue behavior and failure mechanisms of direct laser deposited Ti–6Al–4V, Materials Science and Engineering: A. 655 (2016) 100–112. https://doi.org/10.1016/j.msea.2015.12.026.

[38]   J. Yu, M. Rombouts, G. Maes, F. Motmans, Material Properties of Ti6Al4V Parts Produced by Laser Metal Deposition, Physics Procedia. 39 (2012) 416–424. https://doi.org/10.1016/j.phpro.2012.10.056.

[39]   M.L. Griffith, M.T. Ensz, J.D. Puskar, C.V. Robino, J.A. Brooks, J.A. Philliber, J.E. Smugeresky, W.H. Hofmeister, Understanding the Microstructure and Properties of Components Fabricated by Laser Engineered Net Shaping (LENS), MRS Proc. 625 (2000) 9. https://doi.org/10.1557/PROC-625-9.

[40]   B.E. Carroll, T.A. Palmer, A.M. Beese, Anisotropic tensile behavior of Ti–6Al–4V components fabricated with directed energy deposition additive manufacturing, Acta Materialia. 87 (2015) 309–320. https://doi.org/10.1016/j.actamat.2014.12.054.

[41]   P.S. Korinko, T.M. Adams, S.H. Malene, D. Gill, J. Smugeresky, Laser Engineered Net Shaping® for Repair and Hydrogen Compatibility, (n.d.) 12.

[42]   A.J. Pinkerton, W. Wang, L. Li, Component repair using laser direct metal deposition, Proceedings of the Institution of Mechanical Engineers, Part B: Journal of Engineering Manufacture. 222 (2008) 827–836. https://doi.org/10.1243/09544054JEM1008.

[43]   W. Liu, J.N. DuPont, Fabrication of functionally graded TiC/Ti composites by Laser Engineered Net Shaping, Scripta Materialia. 48 (2003) 1337–1342. https://doi.org/10.1016/S1359-6462(03)00020-4.

[44]   A. Bandyopadhyay, B.V. Krishna, W. Xue, S. Bose, Application of Laser Engineered Net Shaping (LENS) to manufacture porous and functionally graded structures for load bearing implants, J Mater Sci: Mater Med. 20 (2009) 29–34. https://doi.org/10.1007/s10856-008-3478-2.

[45]   G.J. Marshall, W.J. Young, S.M. Thompson, N. Shamsaei, S.R. Daniewicz, S. Shao, Understanding the Microstructure Formation of Ti-6Al-4V During Direct Laser Deposition via In-Situ Thermal Monitoring, JOM. 68 (2016) 778–790. https://doi.org/10.1007/s11837-015-1767-z.

[46]   A. Yadollahi, N. Shamsaei, S.M. Thompson, D.W. Seely, Effects of process time interval and heat treatment on the mechanical and microstructural properties of direct laser deposited 316L stainless steel, Materials Science and Engineering: A. 644 (2015) 171–183. https://doi.org/10.1016/j.msea.2015.07.056.

[47]   S.M. Kelly, S.L. Kampe, Microstructural evolution in laser-deposited multilayer Ti-6Al-4V builds: Part II. Thermal modeling, Metall and Mat Trans A. 35 (2004) 1869–1879. https://doi.org/10/bhbj7h.

[48]   C. Qiu, G.A. Ravi, C. Dance, A. Ranson, S. Dilworth, M.M. Attallah, Fabrication of large Ti–6Al–4V structures by direct laser deposition, Journal of Alloys and Compounds. 629 (2015) 351–361. https://doi.org/10.1016/j.jallcom.2014.12.234.

[49] J.S. Keist, T.A. Palmer, Role of geometry on properties of additively manufactured Ti-6Al-4V structures fabricated using laser based directed energy deposition, Materials & Design. 106 (2016) 482–494. https://doi.org/10.1016/j.matdes.2016.05.045.

[50] A. Vasinonta, J. Beuth, M. Griffith, Process Maps for Laser Deposition of Thin-Walled Structures, Proceedings of the 10th Solid Freeform Fabrication Symposium. (1999) 383–392.

[51] J. Beuth, N. Klingbeil, The role of process variables in laser-based direct metal solid freeform fabrication, JOM. 53 (2001) 36–39. https://doi.org/10.1007/s11837-001-0067-y.

[52] A.C. Nunes, An Extended Rosenthal Weld Model, Welding. (1983) 165s–170s.

[53] N.W. Klingbeil, S. Bontha, C.J. Brown, D.R. Gaddam, P.A. Kobryn, H.L. Fraser, J.W. Sears, Effects of Process Variables and Size Scale on Solidification Microstructure in Laser-Based Solid Freeform Fabrication of Ti-6Al-4V, in: Solid Freeform Fabrication Symposium, Austin, TX, 2004: pp. 92–103. https://sffsymposium.engr.utexas.edu/Manuscripts/2004/2004-10-Klingbeil.pdf.

[54] J. Gockel, N. Klingbeil, S. Bontha, A Closed-Form Solution for the Effect of Free Edges on Melt Pool Geometry and Solidification Microstructure in Additive Manufacturing of Thin-Wall Geometries, Metall and Materi Trans B. 47 (2016) 1400–1408. https://doi.org/10/gf3jzv.

[55] O. Nenadl, V. Ocelík, A. Palavra, J.Th.M.D. Hosson, The Prediction of Coating Geometry from Main Processing Parameters in Laser Cladding, Physics Procedia. 56 (2014) 220–227. https://doi.org/10.1016/j.phpro.2014.08.166.

[56] A.J. Pinkerton, An analytical model of beam attenuation and powder heating during coaxial laser direct metal deposition, J. Phys. D: Appl. Phys. 40 (2007) 7323–7334. https://doi.org/10.1088/0022-3727/40/23/012.

[57] J.C. Heigel, P. Michaleris, E.W. Reutzel, Thermo-mechanical model development and validation of directed energy deposition additive manufacturing of Ti–6Al–4V, Additive Manufacturing. 5 (2015) 9–19. https://doi.org/10.1016/j.addma.2014.10.003.

[58] M.F. Gouge, J.C. Heigel, P. Michaleris, T.A. Palmer, Modeling forced convection in the thermal simulation of laser cladding processes, Int J Adv Manuf Technol. 79 (2015) 307–320. https://doi.org/10.1007/s00170-015-6831-x.

[59] Q. Ye, S. Chen, Numerical Modeling of Metal-Based Additive Manufacturing Process Using Level Set Methods, in: Volume 1: Processes, ASME, Los Angeles, California, USA, 2017: p. V001T02A035. https://doi.org/10.1115/MSEC2017-2939.

[60] A. Fathi, E. Toyserkani, A. Khajepour, M. Durali, Prediction of melt pool depth and dilution in laser powder deposition, J. Phys. D: Appl. Phys. 39 (2006) 2613–2623. https://doi.org/10.1088/0022-3727/39/12/022.

[61] Z. Luo, Y. Zhao, A survey of finite element analysis of temperature and thermal stress fields in powder bed fusion Additive Manufacturing, Additive Manufacturing. 21 (2018) 318–332. https://doi.org/10.1016/j.addma.2018.03.022.

[62]   S.K. Everton, M. Hirsch, P. Stravroulakis, R.K. Leach, A.T. Clare, Review of in-situ
        process monitoring and in-situ metrology for metal additive manufacturing, Materials &
        Design. 95 (2016) 431–445. https://doi.org/10.1016/j.matdes.2016.01.099.

[63]   S. Berumen, F. Bechmann, S. Lindner, J.-P. Kruth, T. Craeghs, Quality control of laser-
        and powder bed-based Additive Manufacturing (AM) technologies, Physics Procedia. 5
        (2010) 617–622. https://doi.org/10/fhkf46.

[64]   Z. Yan, W. Liu, Z. Tang, X. Liu, N. Zhang, M. Li, Review on thermal analysis in laser-
        based additive manufacturing, Optics and Laser Technology. 106 (2018) 427–441.
        https://doi.org/10.1016/j.optlastec.2018.04.034.

[65]   G.J. Marshall, S.M. Thompson, N. Shamsaei, Data indicating temperature response of
        Ti–6Al–4V thin-walled structure during its additive manufacture via Laser Engineered
        Net Shaping, Data in Brief. 7 (2016) 697–703. https://doi.org/10/gf3jzs.

[66]   S.H. Seifi, W. Tian, H. Doude, M.A. Tschopp, L. Bian, Layer-Wise Modeling and
        Anomaly Detection for Laser-Based Additive Manufacturing, Journal of Manufacturing
        Science and Engineering. 141 (2019) 081013. https://doi.org/10.1115/1.4043898.

[67]   G.J. Marshall, S.M. Thompson, S.R. Daniewicz, N. Shamsaei, Estimating the Effects of
        Part Size on Direct Laser Deposition Parameter Selection via a Thermal Resistance
        Network Approach, (n.d.) 15.

[68]   S. Liu, P. Farahmand, R. Kovacevic, Optical monitoring of high power direct diode laser
        cladding, Optics & Laser Technology. 64 (2014) 363–376.
        https://doi.org/10.1016/j.optlastec.2014.06.002.

[69]   J.E. Craig, T. Wakeman, R. Grylls, J. Bullen, Online Imaging Pyrometer for Laser
        Deposition Processing, in: Sensors, Sampling, and Simulation for Process Control, John
        Wiley & Sons, Ltd, 2011: pp. 103–110. https://doi.org/10.1002/9781118061800.ch12.

[70]   T.W. Eagar, Temperature Fields Produced by Traveling Distributed Heat Sources, (1983)
        346–355.

[71]   D. Basak, R.A. Overfelt, D. Wang, Measurement of Specific Heat Capacity and
        Electrical Resistivity of Industrial Alloys Using Pulse Heating Techniques, International
        Journal of Thermophysics. 24 (2003) 1721–1733.
        https://doi.org/10.1023/B:IJOT.0000004101.88449.86.

[72]   COMSOL Multiphysics Reference Manual, (n.d.).
        https://doc.comsol.com/5.4/doc/com.comsol.help.comsol/COMSOL_ReferenceManual.p
        df (accessed September 29, 2019).

[73]   C. Kledwig, H. Perfahl, M. Reisacher, F. Brückner, J. Bliedtner, C. Leyens, Analysis of
        Melt Pool Characteristics and Process Parameters Using a Coaxial Monitoring System
        during Directed Energy Deposition in Additive Manufacturing, Materials (Basel). 12
        (2019). https://doi.org/10.3390/ma12020308.

[74]   L. Wang, S. Felicelli, Analysis of thermal phenomena in LENS^{TM} deposition, Materials
        Science and Engineering: A. 435–436 (2006) 625–631. https://doi.org/10/fs7wnk.

[75]   T.L. Bergman, A.S. Lavine, F.P. Incropera, D.P. DeWitt, Fundamentals of Heat and Mass Transfer, 7th Edition Binder Ready Version edition, Wiley, Chichester, 2011.

[76]   Y.S. Muzychka, M.M. Yovanovich, Thermal Resistance Models for Non-Circular Moving Heat Sources on a Half Space, J. Heat Transfer. 123 (2001) 624. https://doi.org/10/fpvqp6.